Journal of Sound and Vibration 642 (2026) 119951

Contents lists available at ScienceDirect

Journal of Sound and Vibration

journal homepage: www.elsevier.com/locate/jsvi

Numerical evaluation of spherical microphone array designs on acoustic images under ideal conditions using conventional and spherical harmonic beamforming

Kévin Rouard [a,*], Julien St-Jacques [a], Loïc Forma [a], Loic Boileau [b], Franck Sgard [c], Olivier Doutres [a], Nicolas Quaegebeur [b], Hugues Nélisse [c], François Grondin [b], Thomas Padois [c,*]

[a] Department of Mechanical Engineering, École de technologie supérieure, 1100 Rue Notre Dame O., Montréal, H3C 1K3, Québec, Canada
[b] Institut de recherche Robert-Sauvé en santé et en sécurité du Travail, 505 Boulevard de Maisonneuve O., Montréal, H3A 3C2, Québec, Canada
[c] Université de Sherbrooke, 2500, Boulevard de l'Université, Montréal, J1K 2R1, Québec, Canada

ARTICLE INFO

Keywords:
Spherical microphone arrays
Sound source localization
Beamforming
Simulation analysis

ABSTRACT

Identifying noise sources in the workplace is essential to ensure workers' health and safety. This often relies on advanced acoustic sensing systems. Among these, spherical microphone arrays (SMAs) are widely used due to their capability to localize sound sources across a full three-dimensional space. Commercial SMAs typically employ rigid shells combined with spherical harmonic beamforming, while open SMAs utilize conventional beamforming. Only a limited number have been explored in the literature. Although both commercial and custom-made SMAs are frequently employed in the development of source localization algorithms, the design criteria–such as the choice between an open versus a rigid shell, the number of microphones, the array diameter and the positioning of microphones–remain largely under-investigated. In this study, we address this gap by conducting a comprehensive analysis of over 300,000 SMA configurations to evaluate performance in terms of mainlobe width and mainlobe-to-sidelobe ratio. The methodology involves ranking simulated SMA configurations over a broad range of operational frequencies, enabling us to identify key performance trade-offs and critical design parameters. The results offer practical guidelines for designing and selecting SMA configurations that optimize beamforming performance based on specific application requirements, such as the number of microphones, the frequency range, and the chosen beamforming algorithm. The comprehensive codebase, made available together with the analysis reported here, can serve as a benchmark for future studies, promoting more informed decisions in the design and implementation of advanced SMAs.

1. Introduction

Spherical microphone arrays (SMAs) have been extensively used for acoustic imaging in a wide range of applications, including noise source identification in workplaces [1], vehicles [2], and aircraft [3].

* Corresponding authors.
E-mail addresses: kevin.rouard.1@ens.etsmtl.ca (K. Rouard), julien.st-jacques.1@ens.etsmtl.ca (J. St-Jacques), loic.forma@etsmtl.ca (L. Forma), loic.boileau@usherbrooke.ca (L. Boileau), franck.sgard@irsst.qc.ca (F. Sgard), olivier.doutres@etsmtl.ca (O. Doutres), nicolas.quaegebeur@usherbrooke.ca (N. Quaegebeur), hugues.nelisse@irsst.qc.ca (H. Nélisse), francois.grondin2@usherbrooke.ca (F. Grondin), thomas.padois@irsst.qc.ca (T. Padois).

https://doi.org/10.1016/j.jsv.2026.119951
Received 23 May 2025; Received in revised form 2 June 2026; Accepted 7 June 2026
Available online 9 June 2026

These arrays, through the use of beamforming algorithms, enable the localization of sound sources in all directions, creating an acoustic image that visually represents the beamformer output level using a color map, overlaid on a photograph of the recorded environment.

For a more detailed discussion of the performance and applications of beamforming in acoustic imaging, readers can refer to a comprehensive review of the literature, covering both theoretical and practical cases, including noisy conditions [4].

Two types of SMAs are identified in the literature: open and rigid. For open SMAs, the microphones are mounted on a wire frame [5] or rods [1,6–8], while for rigid SMAs, the microphones are flush-mounted on the surface of an acoustically reflective shell. Open SMAs are considered acoustically transparent and do not interfere with acoustic waves. In contrast, rigid SMAs can generate scattering effects [9–11,50]. The combination of different SMA types has also been explored, including either two open layers [12] or a rigid inner layer paired with an open outer layer [13–15], to enhance robustness and to extend the frequency range.

In the case of an open SMA, conventional beamforming in the frequency domain (CBF), based on a free-field Green's function, is commonly used [16]. Generalized cross-correlation (GCC) in the time domain is also applicable, and both algorithms yield similar acoustic imaging performance [17–19]. Both can also be applied to a rigid SMA, albeit without any correction for scattering effects [18]. To address the scattering effects, spherical harmonic beamforming (SHB) can be used, as described in the literature [20,50]. SHB projects the microphone signals onto an orthogonal basis of spherical harmonic functions before performing beamforming. When applied to rigid SMAs, the decomposition of the signals can remove the influence of diffracted waves. Although SHB can be applied to open SMAs with omnidirectional receivers, it is prone to numerical instabilities at certain frequencies due to division by zero in the Bessel functions involved in the spherical harmonic expansion [18,22]. These instabilities can be mitigated by employing open SMAs with cardioid receivers, dual-layer configurations, or averaging over a frequency band [18,20].

A key distinction between CBF and SHB lies in their performance across various frequency ranges. At low values of the dimensionless frequency parameter kr_a (defined in Section 3.3), CBF produces a wider mainlobe than SHB when localizing a point source [11,18,23,50]. In CBF, the mainlobe width depends on the SMA radius, while in SHB, it is determined by the spherical harmonic truncation order, which is bounded by the maximum order imposed by the array geometry. At high values of the dimensionless frequency parameter kr_a, the CBF performance is influenced by the spacing between microphones : the smaller the distance, the higher the frequency limit. In contrast, the theoretical SHB performance is again limited by the maximum truncation order of the spherical harmonics, which defines the dimensionless upper frequency limit [17,20]. The SMA radius, the number of microphones, and their positions are considered key design parameters.

Some studies have focused on specific SMA geometries, keeping the radius and number of microphones fixed while exploring different algorithms. Several open SMAs have been proposed in the literature. One design features 15 microphones on a sphere with a radius of 0.25 m, using a time-domain algorithm based on GCC [1]. Commercially available open SMAs have also been developed with 48 and 120 microphones, with radii of 0.175 m and 0.3 m, respectively, and using a time-domain algorithm [5]. Another study investigated an open SMA with 6 microphones placed at the center of each face of a cube with a side length of 0.5 m, analyzing the use of arithmetic, geometric, and harmonic means in GCC computation [24]. A compact open SMA with 32 microphones and a 0.075 m radius was introduced using the SHB algorithm [6]. Further investigations explored open SMAs with 14 and 15 microphones on a 0.25 m radius sphere, aiming to enhance acoustic imaging by combining GCC with geometric and energetic criteria [7]. An open SMA consisting of 18 microphones in optimized positions was also designed with a 0.2 m radius [8]. Dual-layer open SMAs have also been considered. One configuration placed 12 microphones across two layers with radii of 0.005 m and 0.05 m, targeting room impulse measurement applications, sound recording, and source localization [12]. The use of rigid SMAs has also been extensively studied. A design with 64 microphones arranged in a *t*-design geometry on a 0.14 m radius sphere evaluated both SHB and CBF performance [50]. Subsequent comparisons using a 20-microphone rigid SMA have confirmed SHB's superior resolution at low frequencies [11]. One commercial implementation of a rigid SMA used in experimental studies featured 54 microphones [3]. To further enhance SHB, the spherical harmonics angularly resolved pressure (SHARP) algorithm was introduced for source pressure level estimation and was implemented on a commercially available rigid SMA with 36 microphones and a 0.0975 m radius [9]. Later, a configuration with 50 microphones was proposed, integrating a filter-and-sum algorithm to improve sidelobe rejection [10]. This same commercial array was used in a comparative study of deconvolution algorithms adapted from planar arrays to SHB, where CLEAN-SC demonstrated superior acoustic imaging performance [25]. Dual-layer rigid configurations have also been tested to extend the measurement range. One such array consisted of two layers of 24 microphones: a rigid layer with a radius of 0.15 m, and an open layer with a radius of 0.4 m [14]. Another used 32 microphones per layer at radii of 0.0163 m and 0.06 m [13], while a third design used layers at 0.028 m and 0.0952 m [15].

Few studies have offered a comprehensive comparison of different SMA geometries, evaluating their impact on performance under similar conditions. One such study evaluated the performance of five open SMAs of constant radius, each equipped with 64 microphones, using the CBF algorithm. The geometries considered were *t*-design, Packing, Covering, Minimum Energy, and Spiral. Among these, the Spiral geometry was found to offer the best performance in terms of mainlobe width and sidelobe level [26]. Another investigation compared three microphone geometries–Equi-angle, Gaussian, and *t*-design–across two sets of microphones for the SHB [27]. Since the number of microphones is constrained by the SMA geometry, the first set consisted of 36, 18, and 12 microphones, respectively, while maintaining a consistent truncation order. The second set included 36, 32, and 36 microphones, maintaining a similar number of microphones. The findings indicated that the *t*-design geometry minimized spatial aliasing errors in the acoustic image and that white noise gain (the ratio of output signal power to input white noise power) depended on the number of microphones rather than the geometry itself.

These examples highlight the variety of SMAs (open or rigid) and their usage parameters. To summarize, radii typically range from 0.05 m to 0.4 m, while the number of microphones varies from 12 to 120. This variation illustrates the lack of consensus on

SMA design. With key parameters varying between studies–often without clearly justified choices–and the vast diversity of SMAs, navigating the selection of a suitable design for an application is challenging. To the authors' knowledge, no study has conducted a comprehensive comparison between CBF and SHB across many SMA designs. These classical algorithms constitute the foundation for many enhanced variants. Parameters such as SMA radius, number of microphones, and array geometries have not been extensively analyzed. Designs, whether commercial or custom-made, often lack detailed justification for these choices. This paper presents a numerical study that systematically compares CBF and SHB for both open and rigid SMAs across a wide range of radii, number of microphones, and geometries to identify key factors in designing an optimal SMA under ideal, noise-free conditions. Performances are evaluated via numerical simulation based on objective criteria, including source-level accuracy, mainlobe width, and sidelobe levels. This numerical investigation lays the groundwork for future experimental validations and studies in more realistic acoustic environments.

The theoretical background of CBF and SHB is presented in Section 2. The methodology, including microphone geometries and objective criteria, is detailed in Section 3. Results are presented and discussed in Section 4, followed by concluding remarks in Section 5.

2. Frequency domain algorithms for acoustic imaging

2.1. Beamforming formulation

Throughout the manuscript, a temporal dependency of the form $e^{i\omega t}$ is assumed. An acoustic image at the angular frequency ω, denoted $\mathbf{A}(\omega)$, is given by the product of the steering matrix $\mathbf{W}(\omega)$ and the cross-spectral matrix $\mathbf{C}(\omega)$ of the acoustic pressure captured by the SMA [16],

$$\mathbf{A}(\omega) = \mathbf{W}^H(\omega)\,\mathbf{C}(\omega)\,\mathbf{W}(\omega), \tag{1}$$

where $(\cdot)^H$ denotes the Hermitian transpose. The acoustic image is obtained from the diagonal of the matrix $\mathbf{A} \in \mathbb{C}^{L\times L}$, where $\mathbf{A}$ is a square matrix, L is the number of points on the scan grid, and $\mathbb{C}$ denotes the field of complex numbers. The definitions and dimensions of $\mathbf{W}$ and $\mathbf{C}$ for CBF and SHB are provided in the following sections.

2.2. Conventional beamforming (CBF)

The steering matrix $\mathbf{W} \in \mathbb{C}^{Q\times L}$, where Q represents the number of microphones, is formed from individual steering vectors for each point on the scan grid indexed by $l = 1, \dots, L$. The steering vector $\mathbf{w}_l \in \mathbb{C}^{Q\times 1}$ is obtained from the left pseudoinverse of the Green's function vector $\mathbf{g}_l \in \mathbb{C}^{Q\times 1}$, which represents the transfer functions between a scan point and microphones $q = 1, \dots, Q$ (see formulation *iii* of [28]),

$$\mathbf{w}_l(\omega) = \mathbf{g}_l \left(\mathbf{g}_l^H \mathbf{g}_l\right)^{-1}, \tag{2}$$

where the elements of $\mathbf{g}_l$ are solutions to the inhomogeneous Helmholtz equation of a point source in a free field and are given by,

$$g_{q,l} = \frac{e^{-ikr_{q,l}}}{4\pi r_{q,l}}, \tag{3}$$

where $i = \sqrt{-1}$ is the imaginary unit, $k = \omega/c$ is the wavenumber with c being the sound speed, and $r_{q,l} = ||\mathbf{r}_q - \mathbf{r}_l||$ represents the Euclidean distance between microphone positions $\mathbf{r}_q$ and scan points $\mathbf{r}_l$. The position vectors are expressed in spherical coordinates $\mathbf{r} = (r, \phi, \theta)$ where the radius r is the distance between the observation point and the origin of the SMA, and spherical angles are the azimuth $\phi \in [-180°, 180°]$ and the colatitude $\theta \in [0°, 180°]$. The cross-spectral matrix, denoted by $\mathbf{C}$, is defined as

$$\mathbf{C}(\omega) = \mathbf{p}(\omega)\mathbf{p}^H(\omega), \tag{4}$$

where $\mathbf{p} \in \mathbb{C}^{Q\times 1}$ is the vector of sound pressures recorded by each microphone in the frequency domain, and $\mathbf{C} \in \mathbb{C}^{Q\times Q}$.

2.3. Spherical harmonic beamforming (SHB)

With the SHB, the steering matrix is expressed in the spherical harmonic domain and $\mathbf{W} \in \mathbb{C}^{(N+1)^2\times L}$, where N represents the truncation order explicitly chosen for the microphone geometry (Chap. 5, [20]). Elements of the steering matrix are defined as,

$$W_{n(n+1)+m,l} = d(N)\, b_n^{-1^*}(r_l, r_q, k)\, Y_n^{m^*}(\theta_l, \phi_l), \tag{5}$$

where the indices n and m refer to the order, with values ranging from 0 to N and the degree with values ranging from $-n$ to n. The SHB gain, $d(N)$, is a scalar that is chosen to be a function of the order, N, given by $d(N) = 4\pi/(N+1)^2$. This gain gives a narrow lobe and therefore the maximum of directivity (see [20] for gain formulations). The symbol $(\cdot)^*$ represents the complex conjugate operator. The radial function b_n is the transfer function between the scanning points r_l (or the source position r_s, see section 2.2) and the microphone positions r_q located on the SMA radius r_a ($r_q = r_a$ for all q) which is either open or rigid. The radial function is given for omnidirectional microphones by [29],

$$\begin{cases} b_n(r_l, r_q, k) = (-i)kh_n^{(2)}(kr_l)j_n(kr_q), & \text{open} \\ b_n(r_l, r_q, k) = (-i)kh_n^{(2)}(kr_l)\left(j_n(kr_q) - \frac{j_n'(kr_q)}{h_n'^{(2)}(kr_q)} h_n^{(2)}(kr_q)\right), & \text{rigid} \end{cases} \tag{6}$$

where $h_n^{(2)}$ is the spherical Hankel function of the second kind and j_n is the spherical Bessel function of the first kind. The operator $(\cdot)'$ designates the derivative of these functions with respect to the variable r. This transfer function applies to spherical waves. Its inverse, b_n^{-1}, is commonly referred to as radial filters and used to compensate for radial dependence in the SHB. In the rigid case, it compensates for the scattering effects. These radial filters tend to greatly amplify low-frequency components, with the effect becoming more pronounced as the order n increases. Practical applications necessitate a strategy to reduce the associated noise, such as Tikhonov regularization [2]. Alternatively, the use of cardioid microphones [22] offers a more limited form of noise control. The order can also be limited to avoid the amplitude increase associated with higher orders by setting $N = \lfloor kr_a \rfloor + 1$ [30]. The general form of the spherical harmonic function Y_n^m is given by,

$$Y_n^m(\theta,\phi) = \sqrt{\frac{2n+1}{4\pi}\frac{(n-|m|)!}{(n+|m|)!}} P_n^{|m|}(\cos\theta) e^{\mathrm{i}|m|\phi}, \tag{7}$$

and P_n^m is the associated Legendre function. Note that Y_n^{-m} is obtained by multiplying the conjugate spherical harmonic function by the Condon-Shortley factor $(-1)^m$. The cross-spectral matrix $\mathbf{C} \in \mathbb{C}^{(N+1)^2 \times (N+1)^2}$ is given by,

$$\mathbf{C}(\omega) = \mathbf{Y}^H \left(\boldsymbol{\alpha}\boldsymbol{\alpha}^T \odot \mathbf{p}\mathbf{p}^H \right) \mathbf{Y}, \tag{8}$$

where $\boldsymbol{\alpha} \in \mathbb{R}^{Q \times 1}$ is a weighting vector that corresponds to the quadrature weights for integration on the SMA (see Tables 1 and 2). The subscript $(\cdot)^T$ denotes the transpose operator, the symbol $\odot$ represents the Hadamard product, and $\mathbf{Y} \in \mathbb{C}^{Q \times (N+1)^2}$ is the spherical harmonic matrix.

3. Methods

3.1. Microphone geometries

Based on a literature review, fifteen microphone geometries are selected for this study. The number of microphones considered ranges from 16 to 64, aiming to align with previous works in the literature. Some geometries allow for the use of any number of microphones; these are referred to as "full set" geometries and include t-design, Minimum Energy, Packing, Covering, Maximal Volume, and Spiral. In contrast, certain geometries are constrained by the inherent limitations of their mathematical definitions, restricting the number of usable microphones. These are referred to as "limited set" geometries and include Equi-angle, Gauss-Legendre, Lebedev, Fliege, B&K, Efficient t-design, L-design, Maximum Determinant, and Fibonacci. A summary of these geometries, along with the number of microphones considered, is presented in Table 1, while Table 2 provides the corresponding standardized truncation orders, additional notes, and relevant literature references. Maximal Volume, Efficient t-design, L-design and the Maximum determinant have not yet been introduced into the field of acoustic imaging as array geometries, to the authors' knowledge.

All microphone geometries can be used with CBF [31], whereas SHB requires special attention to ensure the orthogonality of spherical harmonics is preserved. The value of the truncation order N applied in this SHB depends on the product of the wavenumber with the SMA radius r_a and is expressed as [30]

$$N = \begin{cases} \lfloor kr_a \rfloor + 1, & \text{if } \lfloor kr_a \rfloor + 1 \le N_{\max} \\ N_{\max}, & \text{if } \lfloor kr_a \rfloor + 1 > N_{\max} \end{cases}, \tag{9}$$

where the symbol $\lfloor \cdot \rfloor$ represents the floor function and $N_{\max}$ is the maximal truncation order. The truncation orders used in Table 2 are defined by $N_{\max} = \lfloor \sqrt{Q} \rfloor - 1$ [2], ensuring standardization across array geometries. However, this order can exceed the maximum order supported by the geometry, $N_{\sup}$. Eq. (9) adjusts the truncation with kr_a; the SHB output remains unchanged as long as $N(kr_a) \le N_{\sup}$. When $N(kr_a) > N_{\sup}$, spatial aliasing typically appears; in rare cases it may also yield a narrower mainlobe. In noise-free conditions, the truncation rule in Eq. (9) yields beamforming results that match the ideal point spread functions. Due to its simplicity, it serves as a benchmark and remains applicable in the presence of noise.

The analysis begins with 36 and 50 microphones; however, some geometries cannot accommodate these exact numbers due to constraints in their mathematical formulation. We therefore select the nearest number of microphones for 36 and 50 and refer to these microphone sets as $36^\star$ and $50^\star$. Then, the impact of varying the number of microphones from 16 to 64 is examined. Fig. 1 shows the microphone positions on the spherical surface for the geometries considered with the set of $36^\star$ microphones. Figs. 1.(a) to (e) and (j) to (n) exhibit a uniform or nearly uniform distribution of microphone positions. In Figs. 1.(g), (h) and (i), a regular microphone arrangement is observed. In Figs. 1.(f) and (o), the positions follow a spiral pattern. The Lebedev, Fliege, Efficient t-design, L-design, and Maximum Determinant geometries feature microphones placed at the poles. Microphones located at the poles can create design constraints, as supports are required at the bottom pole to hold the SMA and at the top pole to mount a camera. Rotating the microphones positions resolves the issue.

Microphone positions for the geometries are provided in the supplementary material, which also includes the maximum supported truncation orders, the numerical simulations, and results for one configuration at a time.

3.2. Numerical simulations

Numerical simulations were conducted to compare the performance of SMA designs. The sound field is first generated for all configurations, after which beamforming is applied and evaluated according to acoustic image criteria.

Table 1
The fifteen selected geometries, along with the number of available microphones, result in 156 layouts. A full set is defined as a layout with 16 to 64 microphones in steps of 4, with additional numbers 25, 26, 37, 38, 42, 49, 50, and 62 included to account for the limited set of microphones. The limited set does not include all possible numbers of microphones. The symbol ● represents geometries where the number of microphones is 36 or close to 36, denoted 36⋆, and the symbol ■ represents geometries where the number of microphones is 50 or close to 50, denoted 50⋆.

	Geometries	Q																			
		16	20	24	25	26	28	32	36	37	38	40	42	44	48	49	50	52	56	60	62	64
Full Set	*t*-design	×	×	×	×	×	×	×	●	×	×	×	×	×	×	×	■	×	×	×	×	×
	Min. Energy	×	×	×	×	×	×	×	●	×	×	×	×	×	×	×	■	×	×	×	×	×
	Packing	×	×	×	×	×	×	×	●	×	×	×	×	×	×	×	■	×	×	×	×	×
	Covering	×	×	×	×	×	×	×	●	×	×	×	×	×	×	×	■	×	×	×	×	×
	Max. Volume	×	×	×	×	×	×	×	●	×	×	×	×	×	×	×	■	×	×	×	×	×
	Spiral	×	×	×	×	×	×	×	●	×	×	×	×	×	×	×	■	×	×	×	×	×
Limited Set	Equi-Angle	×							●													■
	Gauss-Leg.							●									■					
	Lebedev					×					●						■					
	Fliege	×			×				●							■						×
	B&K								●								■					
	Eff. *t*-design					×		●					×				■				×	
	L-design							●							■							
	Max. Det.	×			×				●							■						×
	Fibonacci				×					●						■						

Table 2
Among the geometries, two configurations are selected with a number of microphones close to 36 and 50, denoted 36⋆ and 50⋆. The corresponding maximum truncation orders applied with SHB, denoted by N_{max}, are calculated using $N_{max} = \lfloor \sqrt{Q} \rfloor - 1$ [2,30]. The maximum supported order is denoted by N_{sup}; the symbol — indicates that the geometry does not have a defined N_{sup}. The "Notes" column defines the geometries and the associated weights α. The geometries mentioned with equal weights are assumed to have $\alpha_q = \frac{4\pi}{Q}$. (first part).

	Geometries	36⋆			50⋆			Notes	Other References
		Q	$\mathbf{N}_{max}$	$\mathbf{N}_{sup}$	Q	$\mathbf{N}_{max}$	$\mathbf{N}_{sup}$		
Full Set	*t*-design	36	6	4	50	6	5	The quadrature of this geometry is exact for polynomials of degree at most t and has equal weights, such that $\alpha_q = \frac{4\pi}{Q}$ [32]. The *t*-design is one of the most widely used geometries in acoustic imaging when a rigid SMA is considered. The codes are available on Sloane's website [33].	[11,20,50] [26,27,34]
	Min. Energy	36	5	—	50	6	—	This geometry results from minimizing the potential energy of Q points on a sphere [33]. It is assumed that the weights are equal.	[26]
	Packing	36	5	—	50	6	—	This geometry solves a geometric problem, namely the optimal approach to tightly packing equal spheres together. The centers of these spheres serve as microphone positions. No specific weights are provided. As the microphone positions are naturally equidistant, equal weights can be assumed.	[26,33]
	Covering	36	5	—	50	6	—	The covering geometry is derived from the solution to the problem of finding the most effective way to achieve the minimum overlap thickness between spheres without gaps between them [35]. The objective is to minimize the maximum distance between points on the surface of a sphere. The centers of the spheres serve as the microphone positions, and equal weights can also be assumed.	[26,33]
	Max. Volume	36	5	—	50	6	—	The microphone positions are those that maximize the convex hull of a volume defined by Q [36]. The positions are evenly spaced, and it is assumed that the weights are equal.	[26,33]
	Spiral	36	5	—	50	6	—	Named as suggested by Du et al. [26], this geometry is helically arranged following the golden ratio, giving both even and odd number of positions. It is assumed that the weights are equal.	[37,38]

Table 2
(second part)

	Geometries	36⋆			50⋆			Notes	Other References
		Q	$\mathbf{N}_{max}$	$\mathbf{N}_{sup}$	Q	$\mathbf{N}_{max}$	$\mathbf{N}_{sup}$		
Limited Set	Eq. Angle	36	5	2	64	7	3	There are $Q = 4(N_{sup}+1)^2$ positions, with weights $\boldsymbol{\alpha}$, as given in [20].	[21,27]
	Gauss-Leg.	32	4	3	50	6	4	There are $Q = 2(N_{sup}+1)^2$ positions, with weights $\boldsymbol{\alpha}$, as given in [20].	[21,27]
	Lebedev	38	5	4	50	6	5	Constructed by rotating the axes of an octahedron, it results in a limited number of microphones with nearly equal weights assigned to the microphone positions. This geometry has been used in the ambisonic field and performs better than Fliege and *t*-design geometries for sound field reproduction with 50 microphones [34].	[39,40]
	Fliege	36	5	5	49	6	6	Obtained by minimizing the potential energy of points, which are considered as electrical charges [41], resulting in nearly equidistant points. The number of positions is $Q = (N_{sup}+1)^2$, and the weights are nearly equal. Notwithstanding the close definition to Min. Energy, the resulting positions are distinct.	[34,42]
	B&K	36	5	5	50	6	5	The microphones and weights of the Brüel and Kjaer geometry, referred to as B&K geometry, are provided with 36 microphones in the Chu et al. paper [43] (azimuth and colatitude columns are reversed in the reference paper's notation) and with 50 microphones in Moreno's thesis [44].	[9,10,25]
	Eff. *t*-design	32	4	3	50	6	4	The Efficient spherical *t*-design geometries offer an optimal ratio of packing and covering spheres with equal weights, with points arranged either symmetrically or asymmetrically [45]. Here, asymmetric points are simply referred to as Efficient *t*-design.	[42]
	L-design	32	4	3	48	5	4	This geometry is an Efficient spherical *t*-design with equal weights and symmetric points. Fewer positions are available than with asymmetric points. This is referred to as L-design, as Puhle suggested in 2020 [46].	[42]
	Max. Det.	36	5	2	49	6	3	This geometry is optimized to spread out the microphone positions by maximizing the determinant of the positions' Gram matrix. Womersley and Sloane provide the positions with the available $Q = (N+1)^2$ microphones and nearly equal weights [47].	[42]
	Fibonacci	37	5	—	49	6	—	The positions are at nearly equal distances, in opposing spirals following the golden ratio. Equal weights are assumed. The number of positions is exclusively odd.	[37,48]

3.2.1. *Sound field simulations*

The sound source is a monopole positioned at ($\phi_s = 0°, \theta_s = 90°, r_s = 2\,\text{m}$), where its position in the equatorial plane yields invariant results for geometries with uniform microphone distributions and marginal variations in the case of non-uniform distributions. The distance between the source and the receiver is chosen to represent a practical workplace scenario. The source emits pure tones corresponding to 17 third-octave band center frequencies ranging from 200 to 8 000 Hz. Each pure tone has an amplitude corresponding to 94 dB SPL at 1 m. The source strength is calculated as follows: $a = 4\pi p_0 10^{94/20}\ \text{Nm}^{-1}$, where p_0 is the reference acoustic pressure ($p_0 = 2 \times 10^{-5}$ Pa). Free-field conditions are assumed in the numerical simulation to avoid additional lobes due to ground or wall reflections. Additionally, no random noise is added to the microphone signals to focus solely on SMA performance. The SMA radii vary between 0.04 and 0.40 m with a logarithmic step, resulting in 30 distinct radius values. Although the SMA radius varies by up to 20 % of the source distance, its influence on the results remains negligible. The acoustic pressure at the microphone q is denoted by $p_q(r_q, \phi_q, \theta_q)$. It is determined by performing an inverse spherical Fourier transform of the field generated by a monopole source of magnitude a. This process considers the array characteristics through the transfer function $b_n(r_s, r_a, k)$ (open or rigid, see Eq. (6)) [20],

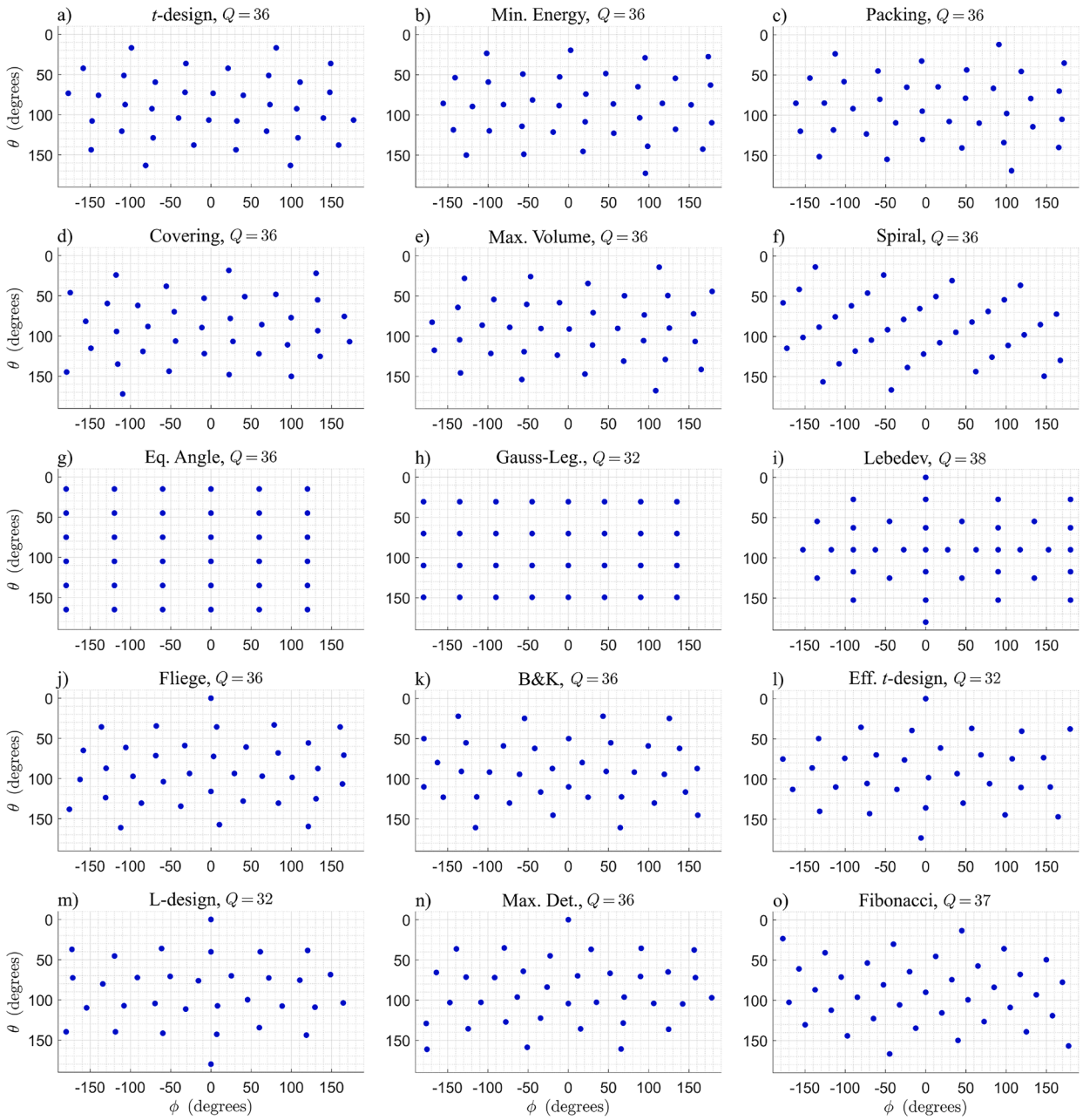

Fig. 1. Positions of the 36⋆-microphone set, represented in the (ϕ,θ) plane.

$$p_q(r_q, \phi_q, \theta_q, k) = a \sum_{n=0}^{N} \sum_{m=-n}^{n} b_n(r_s, r_q, k)\, Y_n^{m^*}(\phi_s, \theta_s) Y_n^m(\phi_q, \theta_q) \tag{10}$$

where the summation is truncated in the computation according to $N = \lceil 1.2kr_a + 8\frac{r_s/(r_a)+1}{r_s/(r_a)} \rceil$, ensuring magnitude errors of approximately 10^{-9} [49], and $\lceil \cdot \rceil$ denotes the ceiling function. The left-hand term imposes a slope of 1.2 with respect to kr_a. The right-hand term ensures a minimum order of $N = 8$ for far-field sources and small array radii (e.g., for $r_s = 2$ m, N varies from 9 to 10 as r_a increases from 0.04 to 0.40 m). This truncation order, restricted to the sound field, aims to balance accuracy and computational cost, as higher orders significantly increase processing time.

3.2.2. Beamforming simulations

The scan zone, where the source is searched, is a grid of 180×90 points distributed equally along the azimuth angle and the colatitude angle at a distance $r_l = 2$ m. The grid density ensures an accurate representation of the main lobe, even for off-grid source

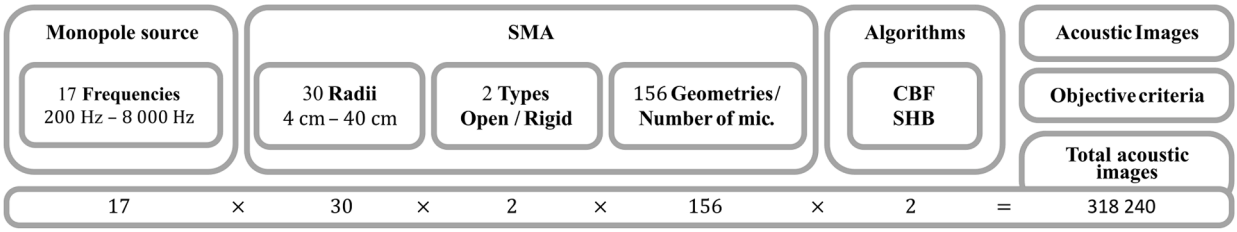

Fig. 2. A total of 318,240 acoustic images is generated from combinations of frequencies, SMA designs, and algorithms.

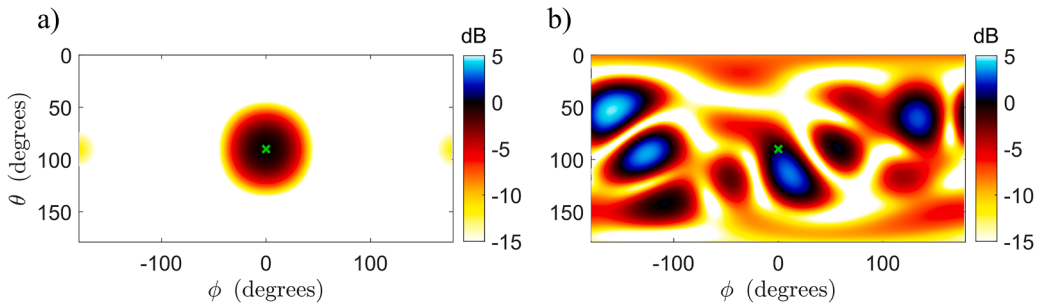

Fig. 3. Illustrative acoustic images displayed with an adapted color scale for positive values, enabling direct discussion of the absolute MLD criterion, with (a) MLD = 0.0 dB and (b) MLD = 4.7 dB. Moreover, in (b), the mainlobe is offset by more than 5° from the expected position (green cross), indicating a source localization error due to spatial aliasing. Note that a high MLD alone does not necessarily imply a localization error. (For interpretation of the references to colour in this figure legend, the reader is referred to the web version of this article.)

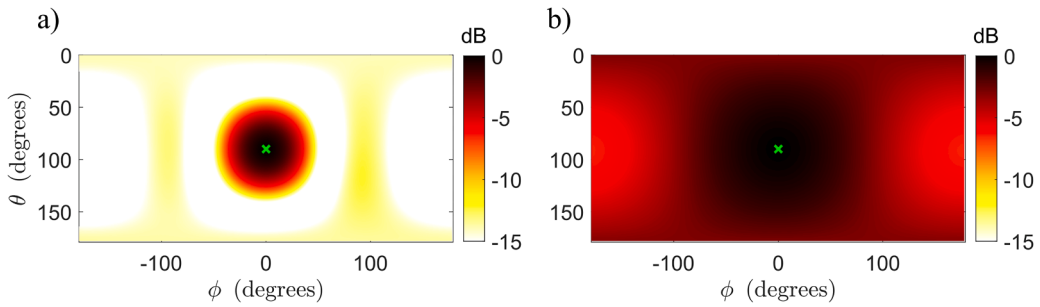

Fig. 4. Illustrative acoustic images with (a) a narrow mainlobe with weak sidelobes, resulting in a SAR of 5 %, and (b) a wide mainlobe covering the image, resulting in a SAR of 50 % (exceeding the 30 % threshold).

locations. The acoustic image is then obtained with the CBF or SHB algorithms, respectively. A total of 318,240 acoustic images are generated (see Fig. 2). Consequently, according to the numerical method, the resulting images can be considered the point spread function of the SMA.

3.3. Performance criteria

To facilitate comparison across different frequencies and array sizes, the results are presented in terms of the dimensionless parameter kr_a. This parameter represents the product of the wavenumber $k = 2\pi f/c$ and the array radius r_a, simplifying the analysis by enabling a direct comparison between different array radii and operating frequencies. The parameter kr_a can be interpreted as follows: for low values of kr_a, typically between 0 and 1.5, a low-frequency range is considered, corresponding to small SMAs relative to the wavelength. Intermediate values of kr_a, ranging from 1.5 to 6, correspond to mid-frequencies. High values of kr_a, from 6 to 16, indicate a high-frequency range and are typically obtained with large SMAs relative to the wavelength. Table A.1 (see Appendix A) provides a reference for converting kr_a to physical values of frequency and radius, helping to estimate the practical operational range of the array.

The influence of the SMA designs is first analyzed using the mainlobe level difference (MLD, Section 3.3.1), the solid angle ratio (SAR, Section 3.3.2), and the mainlobe-to-sidelobe ratio (MSR, Section 3.3.3). Lastly, the effect of the number of microphones, ranging from 16 to 64, on the MSR distribution is evaluated using boxplots. This last analysis is conducted with a linear kr_a step of 0.05, considering the minimum, maximum, and mean MSR values.

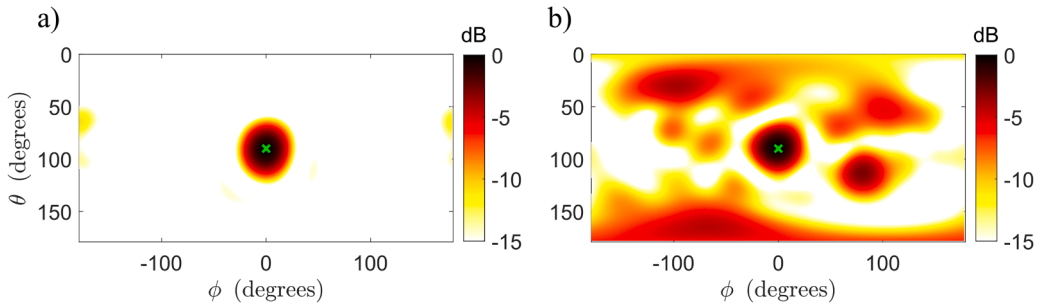

Fig. 5. Illustrative acoustic images with (a) a mainlobe with one weak sidelobe, resulting in an MSR of 10.9 dB (> 6 dB), and (b) a mainlobe with many strong sidelobes, resulting in an MSR of 2.8 dB (< 6 dB).

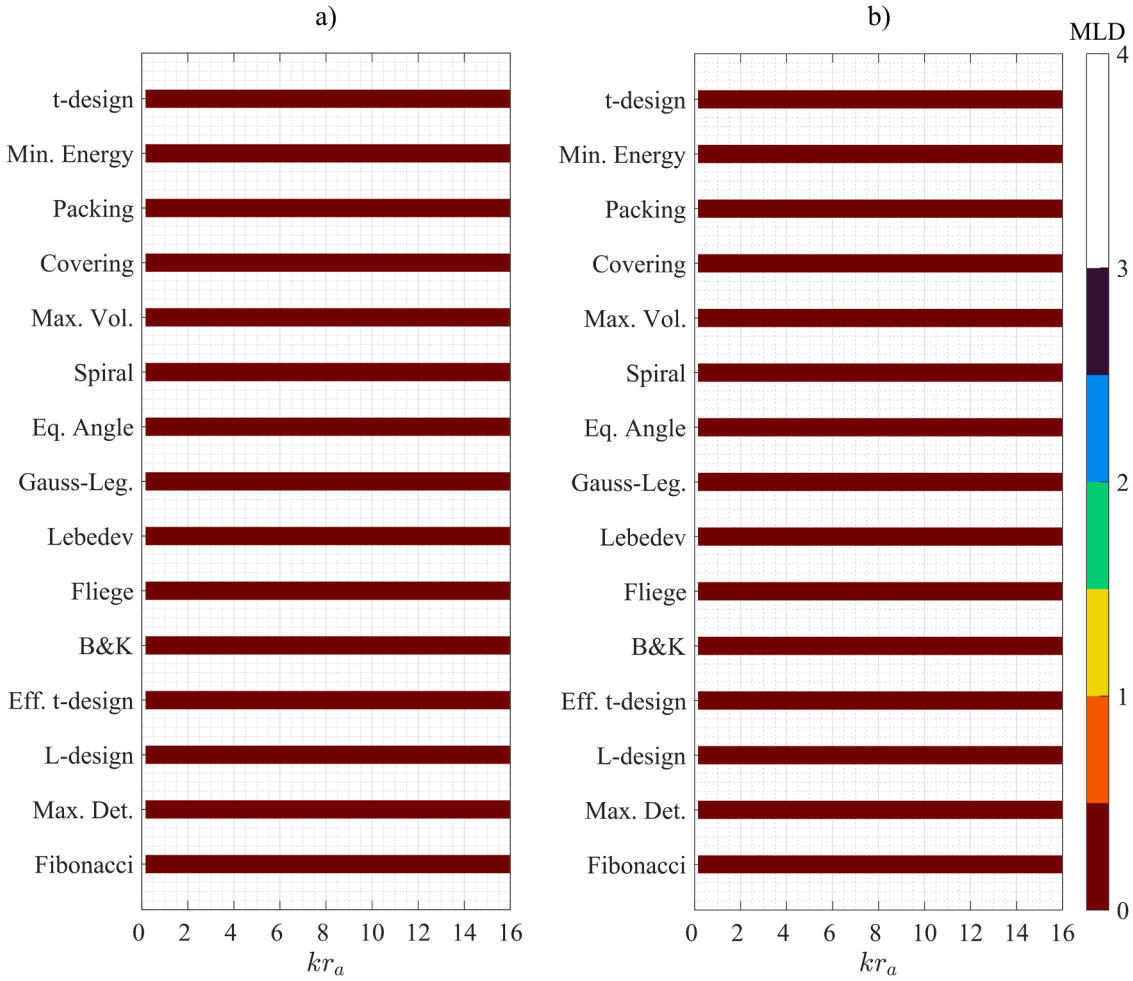

Fig. 6. MLD obtained with the CBF algorithm and open SMAs for the (a) 36*- and (b) 50*-microphone sets, respectively (see Table 1).

3.3.1. Mainlobe level difference (MLD)

For a monopole source, an acoustic image is a combination of a desired mainlobe and undesired sidelobes. The mainlobe indicates the source position, while the sidelobes are artifacts due to the SMA geometry and the selected algorithm. The mainlobe peak value provides the strength level of the source, and the MLD criterion serves as an indicator of the error in the estimated strength level [1,9,28]. The estimated strength level L_e is based on the maximum over the diagonal elements of $\mathbf{A}$ (see Eq. (1)): $L_e = 10\log_{10}\left(\max\left(\mathbf{A}_{ll}\right)\right)$. Therefore, L_e corresponds to the peak value of the acoustic image. The reference strength level, designated as L_r, is calculated as $L_r = 10\log_{10}\left(a^2\right)$. The MLD is obtained by $\mathrm{MLD} = |L_e - L_r|$, where $|\cdot|$ denotes the absolute value. In the figures presented in the

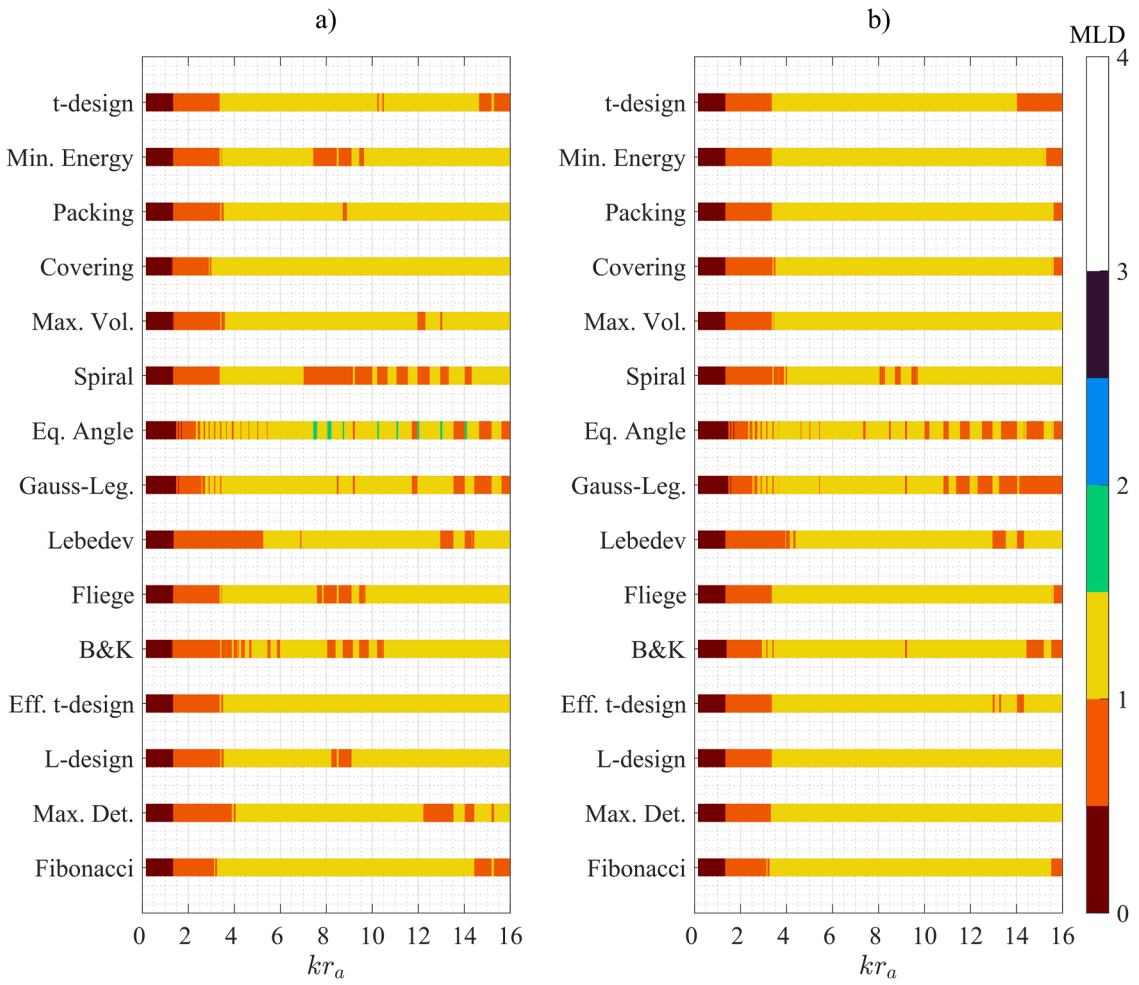

Fig. 7. MLD obtained with the CBF algorithm and rigid SMAs for the (a) 36⋆- and (b) 50⋆-microphone sets, respectively (see Table 1).

results section, when the estimated source position deviates by more than 5° in either azimuth or colatitude from the true position, a magenta dot is added to the plot to indicate a source localization error. Fig. 3 shows acoustic images illustrating the MLD criterion.

3.3.2. *Solid angle ratio (SAR)*

In acoustic imaging, the nature of the mainlobe is crucial, as it is used to determine both the position of the sound source and the sound level. A narrower mainlobe enhances the accuracy of source localization. The mainlobe of a linear microphone array is characterized by its full width at half maximum (FWHM), measured from the peak value to the −3 dB point. With a 2D microphone array, the mainlobe can be characterized by its FWHM or area [17,51]. When using SMAs, the mainlobe may be characterized within a spherical representation. In an attempt to characterize the mainlobe, a criterion based on the solid angle Ω is used [52],

$$\Omega = \int_{-\pi}^{\pi} \int_{-1}^{1} \chi(\phi_l, \theta_l)\, \mathrm{d}(\cos\theta_l)\mathrm{d}\phi_l, \tag{11}$$

where d denotes the differential operator, and $\chi(\phi_l, \theta_l)$ is a binary mask that accepts only the pixels in the acoustic image, defined as,

$$\chi(\phi_l, \theta_l) = \begin{cases} 1 & \text{if the level is} \geq -3\,\text{dB from the peak value,} \\ 0 & \text{otherwise.} \end{cases} \tag{12}$$

The solid angle is normalized by the total solid angle of a sphere (4π), yielding the SAR, $\overline{\Omega} = \Omega/4\pi$, expressed as a percentage. A sufficiently narrow mainlobe is defined as having a value of less than 30 %, while a higher value indicates that the mainlobe is too wide (see Fig. 4). Even though the ability to separate two sources is not studied here, it can still be inferred from the data in relation to the size of the mainlobe (the smaller the mainlobe, the greater the separation capacity). In the figures presented in the results section, a magenta dot is added to the plot to indicate a source localization error greater than 5° in either azimuth or colatitude. In

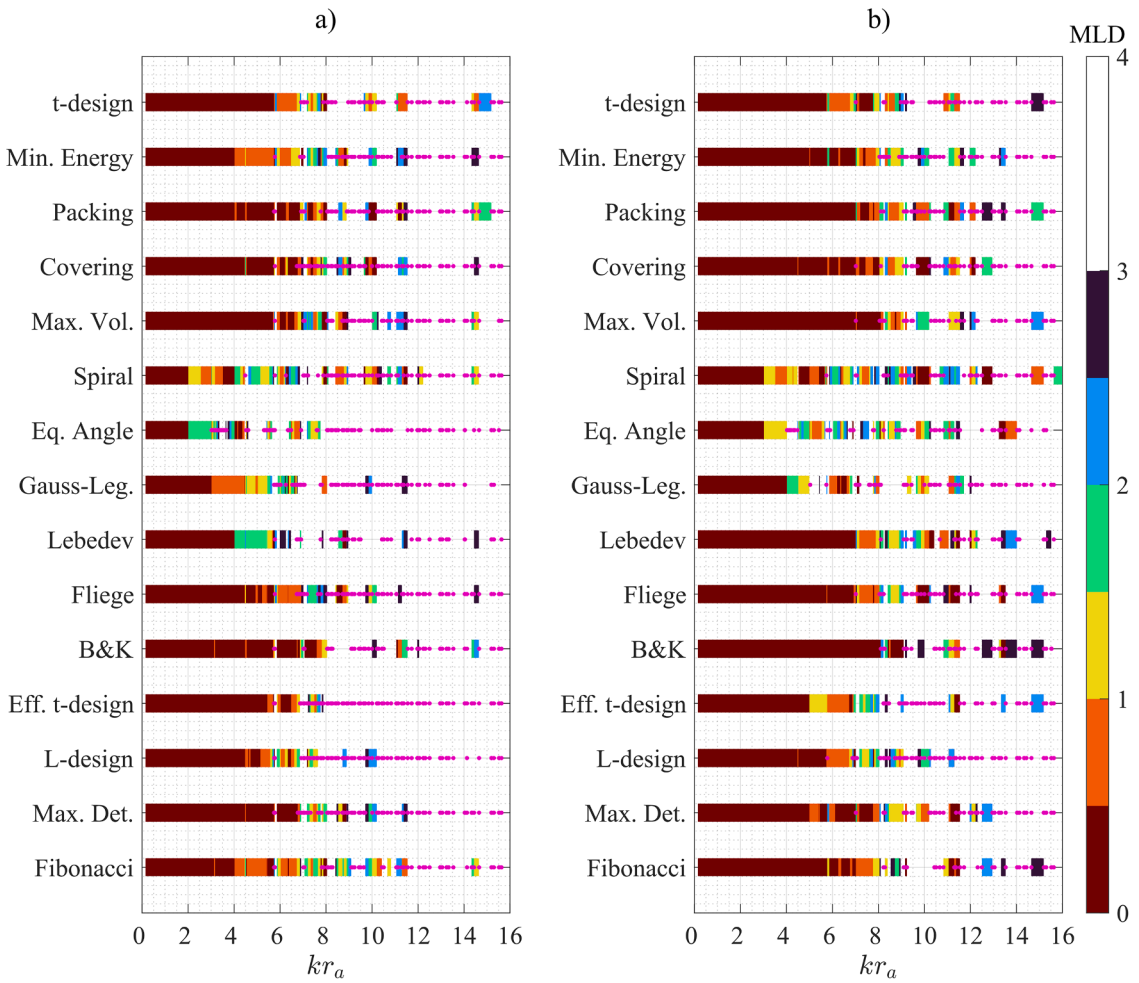

Fig. 8. MLD obtained with the SHB algorithm and open SMAs for the (a) 36⋆- and (b) 50⋆-microphone sets, respectively (see Table 1). Magenta dots indicate errors of $+5°$ in the azimuth or colatitude angles between the mainlobe and the source position.

certain cases, sidelobes may contribute to the SAR if their level exceeds the -3 dB threshold. The MSR, introduced previously, can reveal whether this occurs.

3.3.3. Mainlobe-to-sidelobe ratio (MSR)

Sidelobes are one or more secondary peaks present in the acoustic image. The maximum level excluding the mainlobe is denoted L_s. When a sidelobe exhibits a high level, it may be misinterpreted as an acoustic source, which is an undesired outcome. The MSR, defined by $L_e - L_s$, characterizes the algorithm's ability to minimize the sidelobe relative to the mainlobe [4]. Local maxima were extracted using the `peaks2` function in MATLAB [53], which provides improved detection of sidelobes compared to `findpeaks`. An MSR with a high value results from a low sidelobe level in the acoustic image [9], thus facilitating more accurate identification of the source [17]. An MSR below 6 dB is considered the threshold for rejecting an acoustic image (see Fig. 5). Accordingly, red dots are added in the figures in the results section to indicate configurations with MSR < 6 dB. Magenta dots indicate cases where no sidelobes are detected and the MSR is therefore undefined. In such circumstances, the SAR provides a viable alternative for evaluating performance.

4. Results

The influence of SMA designs on acoustic imaging is first evaluated with the 36⋆- and 50⋆-microphone sets, based on the MLD (Section 4.1), SAR (Section 4.2), and MSR (Section 4.3). Recall that the labels 36⋆ and 50⋆ are used as convenient designations for the microphone sets, although they do not reflect the exact number of microphones, which depends on the geometry (see Table 1). The selected SMA designs are then evaluated in Section 4.4 using the MSR distribution ranging from 16 to 64 microphones.

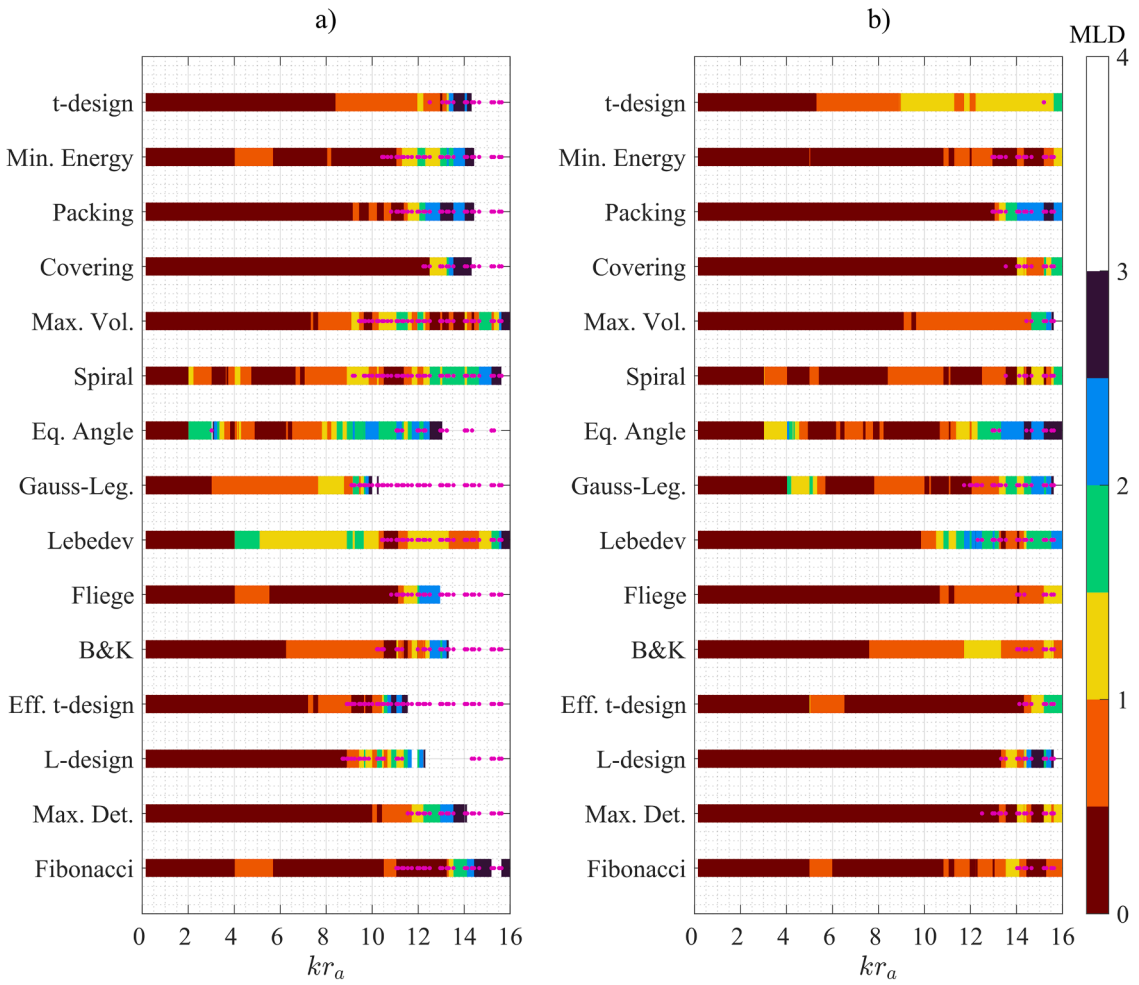

Fig. 9. MLD obtained with the SHB algorithm and rigid SMAs for the (a) 36⋆- and (b) 50⋆-microphone sets, respectively (see Table 1). Magenta dots indicate errors of +5° in the azimuth or colatitude angles between the mainlobe and the source position.

4.1. Influence of the SMA design on the MLD

4.1.1. MLD Obtained with CBF

Figs. 6 and 7 display the MLD obtained with the CBF for open and rigid SMAs, respectively, for all microphone geometries as a function of kr_a. The MLD colorbar ranges from 0 to 3 dB; the values outside this range are colored in white.

As illustrated in Fig. 6, the MLD for the open SMAs is close to zero. These results demonstrate that the geometry, across the kr_a range, has no effect on the MLD with the CBF and open SMAs for 36⋆ and 50⋆ microphones.

In Fig. 7, the MLD for rigid SMAs remains close to zero for $kr_a < 1.5$, indicating a negligible scattering effect within the low-frequency range. For $kr_a > 1.5$, all MLD values increase, reaching 1 dB for every geometry above $kr_a = 4$. Above $kr_a = 4$, geometries with 36⋆ microphones show a slight reduction in MLD compared to those with 50⋆ microphones. The Equi-Angle geometry with 36⋆ microphones yields a higher value of 2 dB. The rigid type of SMA is known to induce scattering effects that perturb the acoustic field, increasing acoustic pressure at the front of the SMA while creating a shadow zone at the rear. This effect is not compensated by the CBF algorithm, as it relies on the free-field Green's function, leading to inaccurate estimation of the source level with a rigid SMA. This discrepancy explains the differences observed between open and rigid SMAs.

No errors in mainlobe position were detected regardless of the array design or the number of microphones. In conclusion, the CBF exhibits better MLD performance with open SMAs than with rigid ones, as its steering vector is based on a free-field Green's function. Therefore, the CBF will not be considered with rigid SMAs; henceforth, when the CBF is referenced, the SMA is presumed to be open.

4.1.2. MLD Obtained with SHB

Fig. 8 and 9 display the MLD obtained with the SHB for open and rigid SMAs, respectively, for all geometries comprising the 36⋆- and 50⋆-microphone sets as a function of kr_a. A deviation of the mainlobe from the expected source position with an angular error of 5°, irrespective of azimuth or colatitude is represented by a magenta dot in the figures.

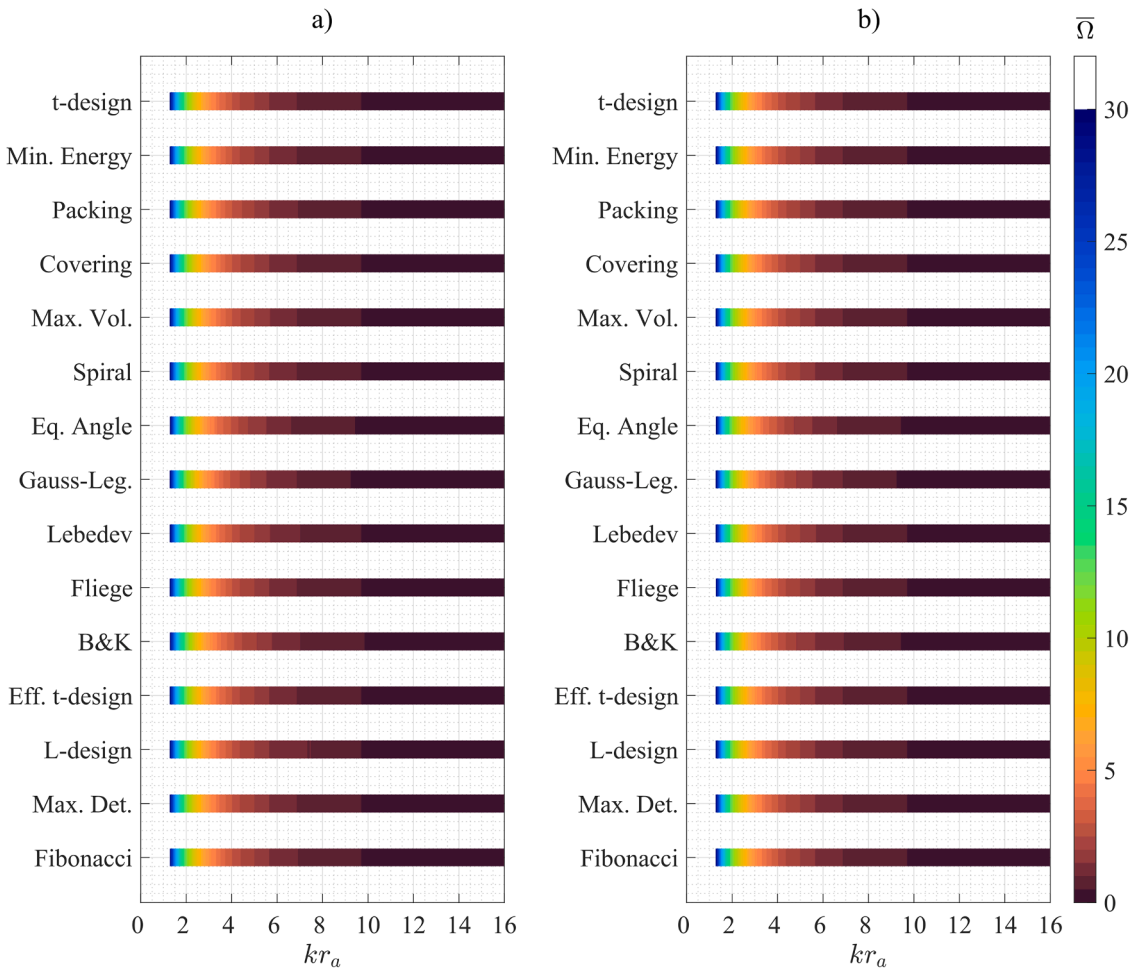

Fig. 10. SAR obtained with the CBF algorithm and open SMAs for the (a) 36⋆- and (b) 50⋆-microphone sets, respectively (see Table 1).

Fig. 8 illustrates the results obtained with the open SMAs. A deviation error of 5° is commonly observed due to sidelobes for $kr_a > 3$. The overestimation of MLD observed at $kr_a = 5.8$, 7, and 8.2 is attributed to a division by zero given by the Bessel function (see Eq. (6)). For $kr_a \geq 5.8$, no geometry with 36⋆ microphones achieves acceptable MLD values in the high-frequency range. Similarly, with 50⋆ microphones, no geometries achieve acceptable MLD values for $kr_a \geq 7$, except for the B&K, which maintains acceptable performance up to $kr_a = 8$.

Fig. 9 illustrates the results obtained with the rigid SMAs. Fewer magenta dots are present compared to the open SMAs, indicating that the source localization error is less prevalent. These are mainly observed for $kr_a > 9$ with the 36⋆-microphone geometries and for $kr_a > 12$ with the 50⋆-microphone geometries. The MLD increases when there is a localization error. A variation of ± 2 dB in the MLD of the Equi-angle geometry at $kr_a = 3$ and $kr_a = 4$ is observed with the 36⋆- and 50⋆-microphone sets, respectively. This corresponds to $N_{\text{sup}} + 1$, of the Equi-angle geometry, showing its limit.

In conclusion, the SHB leads to a better MLD with rigid SMAs than with open ones, as there is no null value with the Bessel functions. The Equi-angle and Gauss-Legendre geometries yield the worst results, regardless of the number of microphones (36⋆ or 50⋆) and the SMA type (open or rigid). The Spiral geometry is ineffective when used with an open SMA.

In contrast to the CBF, the SHB fails to estimate the reference level in the high-frequency range due to spatial aliasing, which typically occurs when $kr_a > N + 1$. For the open case, the SHB is unable to consistently estimate the reference level beyond $N_{\text{max}} + 1$ (see Table 2). However, in the rigid case, the SHB can estimate the reference level beyond this threshold. Moreover, no angular error was observed in the previous results with the CBF. Such errors only appear with the SHB in the high-frequency range. Regardless of the SMA type, increasing the number of microphones naturally raises the maximum supported truncation order, leading to better results in the high-frequency range. In the following, only rigid SMAs are considered with SHB. Moreover, since the Equi-angle and Gauss-Legendre geometries provide the worst MLD with the SHB, they will not be considered in the following sections.

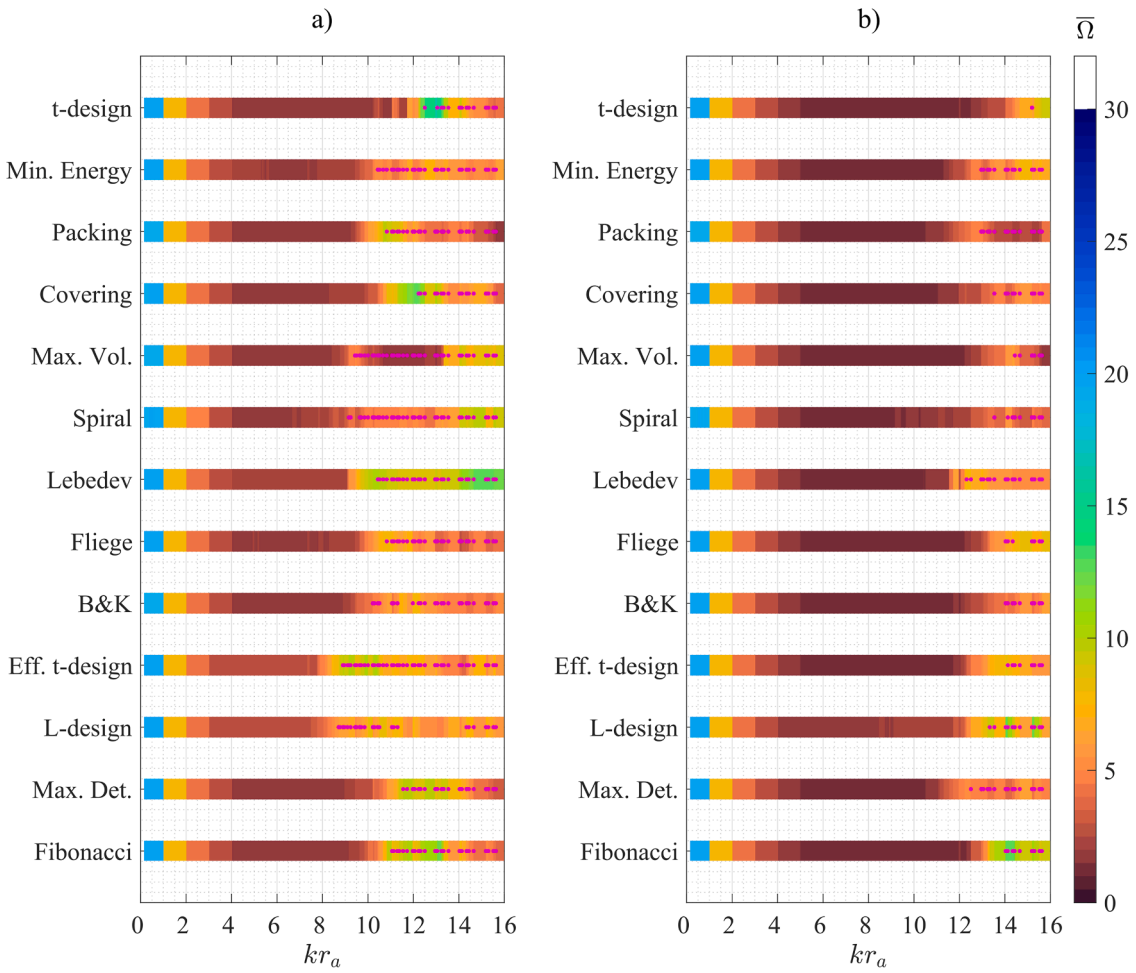

Fig. 11. SAR obtained with the SHB algorithm and rigid SMAs for the (a) 36⋆- and (b) 50⋆-microphone sets, respectively (see Table 1). Magenta dots indicate errors of +5° in the azimuth or colatitude angles between the mainlobe and the source position.

4.2. Influence of the SMA design on the SAR

Figs. 10 and 11 display the SAR obtained with the CBF (open SMAs) and SHB (rigid SMAs) algorithms. Only the SAR values ranging from 0 % to 30 % are shown. Above 30 %, ineffective source localization is likely to occur due to an excessively wide mainlobe. Again, magenta dots indicate source localization errors.

Fig. 10 indicates that with CBF, there is no significant difference between geometries or the number of microphones. Overall, the SAR exceeds the 30 % threshold in the low-frequency range, below $kr_a = 1.3$. When $kr_a \ll 1$, the mainlobe is wide, which is a known limitation of the CBF. As kr_a increases, the SAR value decreases, reaching a mean value of 0.4 % at $kr_a = 10$. The absence of magenta dots in the figures indicates that there is no source localization error, and the mainlobe still aligns with the source position.

Fig. 11 shows that with SHB, the SAR remains identical across different geometries at low kr_a and for different numbers of microphones (36⋆ and 50⋆). The SAR value is on average 19.4 % for $kr_a < 1$ across all configurations and then decreases in a staircase pattern as kr_a increases. This is because the truncation order N is selected as a function of kr_a ($N = \lfloor kr_a \rfloor + 1$), up to $N_{\max}$. The Efficient t-design for 36⋆ microphones and the L-design for both numbers of microphones miss one staircase step due to their low $N_{\sup}$. However, the Maximum Determinant configuration with 36⋆ microphones does not miss this staircase step, even though its $N_{\sup}$ is comparably low. Once N saturates, the SAR values stagnate up to $kr_a = 8$ for the 36⋆-microphone set and up to $kr_a = 12$ for the 50⋆-microphone set. These kr_a values correspond to the point at which localization errors begin to appear. The t-design also achieves the widest range without localization errors (up to $kr_a = 12$ and $kr_a = 15$, respectively). Localization errors coincide with an increase in SAR at high kr_a, caused by the contribution of numerous emerging sidelobes due to spatial aliasing, exceeding the −3 dB threshold.

In conclusion, the SAR is barely affected by the SMA geometry with the CBF across the entire kr_a range, similar to the SHB, except in the high-frequency range, where the truncation order (related to the number of microphones) plays an important role. A wide

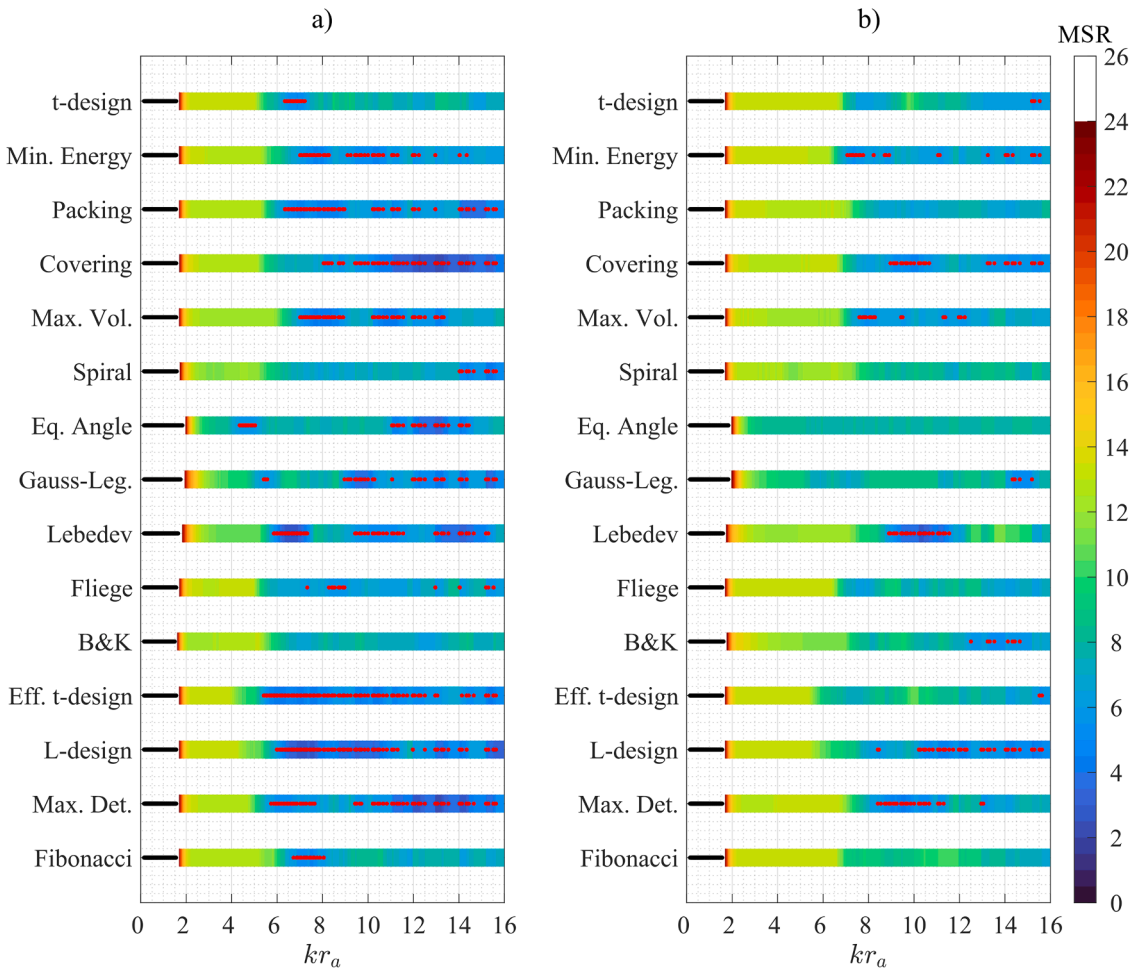

Fig. 12. MSR obtained with the CBF algorithm and open SMAs for the (a) 36⋆- and (b) 50⋆-microphone sets (see Table 1). The red dots correspond to MSR < 6 dB, and black dots indicate that no sidelobes are present in the acoustic image. (For interpretation of the references to colour in this figure legend, the reader is referred to the web version of this article.)

mainlobe occurs at low kr_a, while the mainlobe width reduces as kr_a increases. At high kr_a, the SAR values may increase when using the SHB, due to the contribution of sidelobes. Increasing the number of microphones from 36⋆ to 50⋆ does not influence the SAR with the CBF. With the SHB, source localization errors decrease as the number of microphones increases, coinciding with the rise of the truncation order. The use of the CBF is not recommended below $kr_a = 1.3$, as its SAR exceeds 30 %. Instead, the SHB should be used for $kr_a < 1$ to obtain a smaller SAR.

4.3. *Influence of the SMA design on the MSR*

Figs. 12 and 13 display the MSR obtained with the CBF (open SMAs) and SHB (rigid SMAs) algorithms, respectively. The MSR is plotted in the range [0, 24] dB for each geometry as a function of kr_a. The higher the MSR, the better the performance. The limitation of this statement arises when there are no sidelobes left to define the MSR. In such instances, a black dot indicates both a unique and likely wide mainlobe, as shown in Fig. 12 for $kr_a < 2$. If the MSR is less than 6 dB, the sidelobe level is considered too high, as indicated by a red dot in the plot.

In Fig. 12, the MSR values with the CBF exceed 24 dB for $kr_a < 2$, and are associated with an absence of identifiable sidelobes, due to a wide mainlobe spanning the majority of the acoustic image (SAR above 30 %, see Fig. 10). Above $kr_a = 2$, the MSR stabilizes around 13.2 dB over an extended kr_a range before gradually decreasing for all geometries. Among them, the Equi-angle and Gauss-Legendre geometries, for the 36⋆- and 50⋆-microphone sets, show sidelobes at $kr_a = 2$, whereas sidelobes emerge for the other geometries around $kr_a = 1.7$. This shift in sidelobe visibility does not indicate a significant improvement, since the MSR remains high and the mainlobe is still as wide as for the other geometries (see Fig. 10). Moreover, after this point, these geometries exhibit the steepest decrease in MSR values, indicating a faster degradation compared to the other configurations. When using the 36⋆-microphone set, most geometries exhibit MSR values below 6 dB for $kr_a > 6$, except for the Spiral and B&K geometries. These two geometries maintain

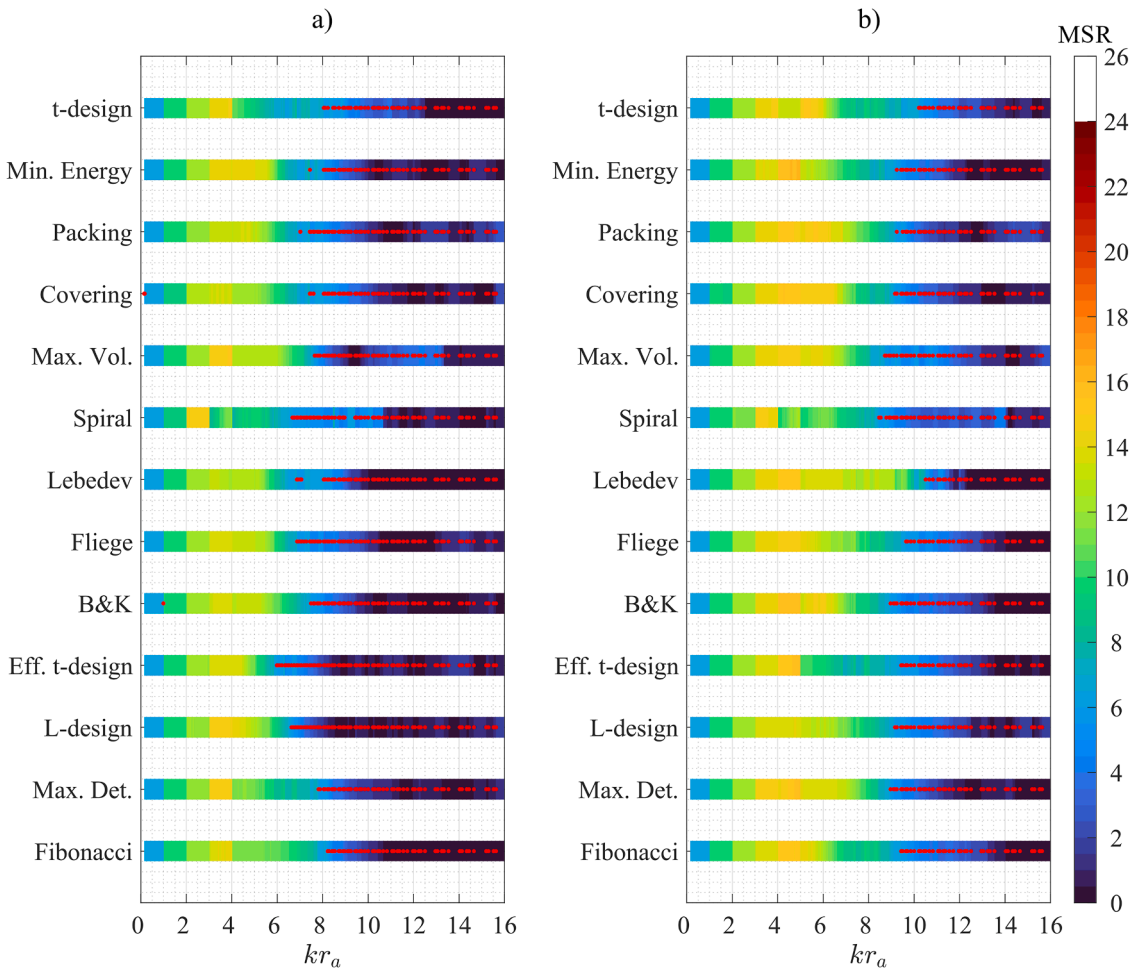

Fig. 13. MSR obtained with the SHB algorithm and rigid SMAs for the (a) 36⋆- and (b) 50⋆-microphone sets (see Table 1). The red dots correspond to MSR < 6 dB. (For interpretation of the references to colour in this figure legend, the reader is referred to the web version of this article.)

MSR values above this threshold, with minimum MSR values of 6.4 and 6.1, respectively, up to $kr_a = 14$ and across the entire kr_a range. The Equi-angle and Gauss-Legendre geometries show inferior performance, as they exhibit MSR values below 6 dB, at kr_a as low as 4 and 5, respectively. Increasing the number of microphones, from 36⋆ to 50⋆, significantly modifies the MSR values. Eight geometries now exhibit similar performance, with high MSR values over the range $kr_a = [2, 14]$: Fliege, *t*-design, Packing, Efficient *t*-design, Fibonacci, and Spiral geometries. Minimum Energy and Maximal Volume show inferior performance with MSR values below 6 dB from around $kr_a = 7$ and higher.

Fig. 13 shows that for $kr_a < 2$, the SHB algorithm exhibits reduced sidelobes compared to the CBF. As a reminder, at this kr_a, the SHB algorithm also exhibits a narrower mainlobe, whereas the CBF's mainlobe covers the entire acoustic image. The MSR is above 6 dB for $kr_a \in [0, 1]$ and increases by 3 dB per unit of kr_a up to $kr_a = 3$ for most geometries, as the truncation order increases. Above $kr_a = 3$, the MSR values depend on the individual geometry then gradually decrease, reaching values below 6 dB (indicated by red dots in the figure). For example, for the Minimum Energy geometry with 50 microphones, the MSR values are approximately [6, 9.6, 12, 14, 16] dB across successive staircase levels. For the 36⋆-microphone sets, the Covering and B&K geometries show an MSR below 6 dB at $kr_a \leq 1$. The Efficient *t*-design and Fibonacci geometries show the smallest and largest kr_a range above the 6 dB threshold up to 6 and 8, respectively. For the 50⋆-microphone set, the MSR range above 6 dB is more extended than in the previous set. The Lebedev geometry provides the widest range above 6 dB, extending up to $kr_a = 10.5$, whereas the Spiral has the smallest range, reaching up to $kr_a = 8.5$.

In conclusion, the geometries have a considerable influence on the MSR. Increasing the number of microphones shows an improvement in the usable kr_a range for each geometry. CBF is not applicable for $kr_a < 2$, and SHB should be used instead below this threshold. The MSR values increase as the truncation order increases. From $kr_a = 2$ to 3, the MSR values are higher with the CBF than with the SHB (by approximately 1 dB). From $kr_a = 3$ to 4, SHB gives higher MSR values than CBF (again by approximately 1 dB), except for Spiral with 36⋆ microphones. This is also observed for $kr_a = 4$ to 5 except for *t*-design and Spiral.

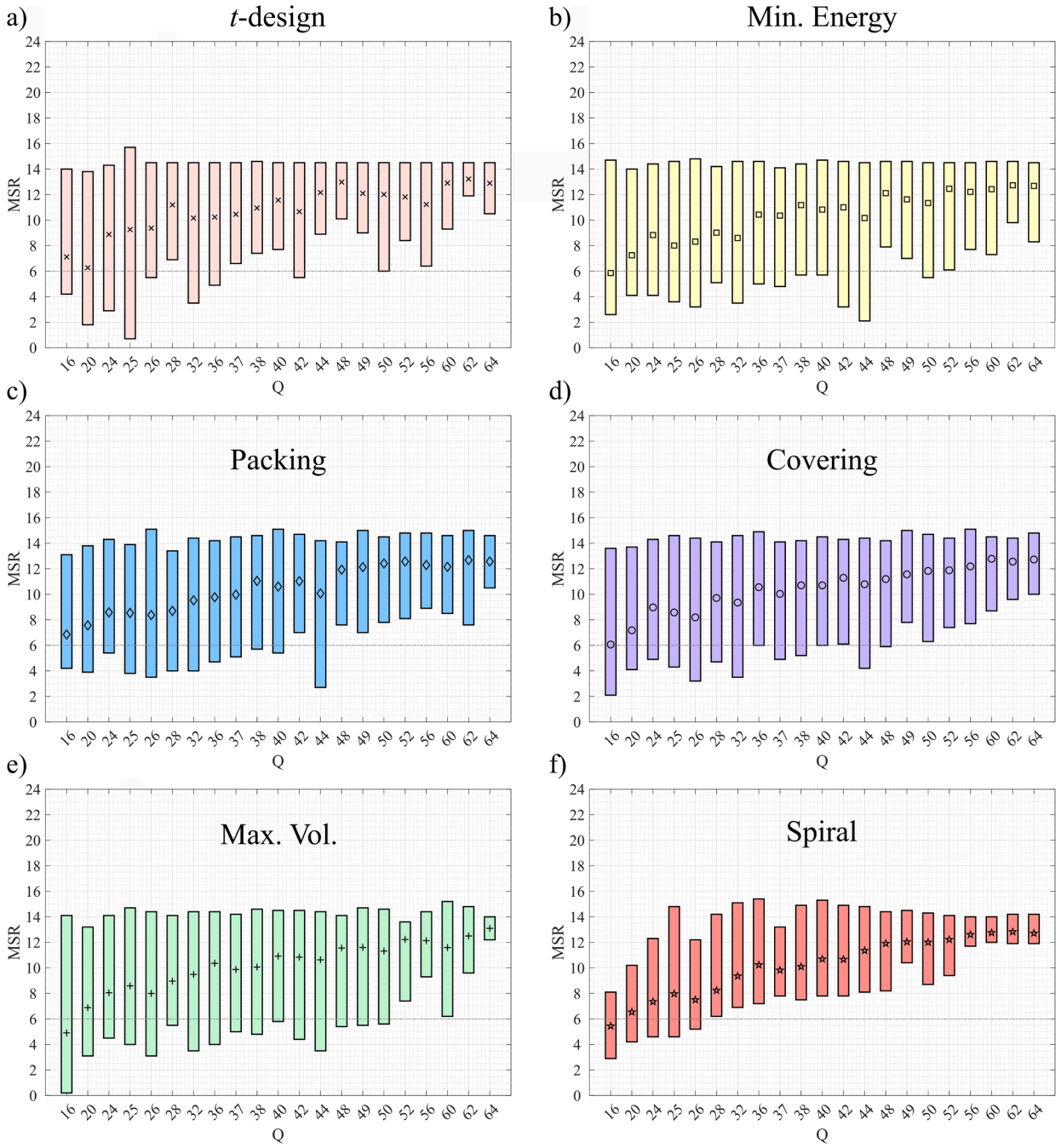

Fig. 14. MSR distribution obtained with the CBF algorithm and open SMAs (full set), as a function of the number of microphones Q: (a) $\times$ t-design, (b) $\square$ Min. Ener., (c) $\diamond$ Packing, (d) $\circ$ Covering, (e) $+$ Max. Vol. and (f) $\star$ Spiral. Gauss-Leg. Lebedev The horizontal dotted line corresponds to MSR = 6 dB.

4.4. Influence of the SMA design on the MSR distribution

In the previous section, the MSR was analyzed as a function of kr_a using the 36⋆- and 50⋆-microphone sets. In this section, the MSR is examined as a function of the number of microphones, ranging from 16 to 64. The MSR values are summarized using a boxplot, where the central symbol represents the arithmetic mean MSR, and the upper and lower edges indicate the minimum and maximum MSR values, respectively. The MSR values are evaluated over a kr_a range defined by previously observed limitations from $kr_a = 2$ (set by the CBF with an open SMA, where the mainlobe is too wide and covers the majority of the acoustic image) to $kr_a = 8$ (set by the

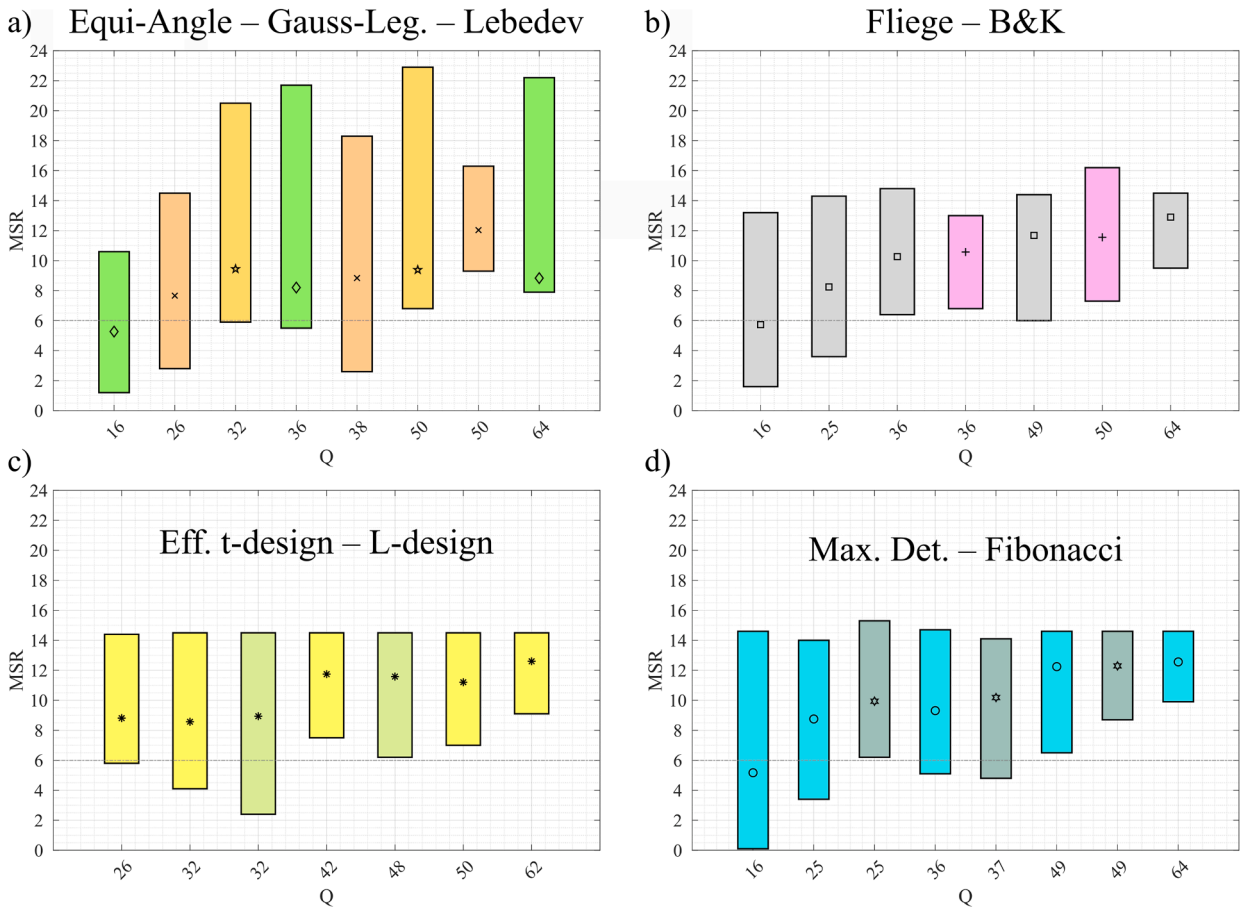

Fig. 15. MSR distribution obtained with the CBF algorithm and open SMAs (limited set), as a function of the number of microphones Q: (a) Eq.-Angle, Gauss-Leg., Lebedev, (b) Fliege, B&K, (c) Eff. t-design, L-design and (d) Max. Det. and Fibonacci. The horizontal dotted line corresponds to MSR = 6 dB.

SHB with a rigid SMA, as most MSR values drop below 6 dB beyond this kr_a). A horizontal dotted line at MSR = 6 dB is included in the Figs. 14 to 17 as a reference threshold. Ideally, the minimum MSR values should remain above this threshold, as values below 6 dB are considered to indicate ineffective beamforming performance. A high maximum MSR value indicates strong performance. An optimal configuration is characterized by a narrow min-to-max MSR range and a minimal number of microphones.

4.4.1. MSR Distribution with CBF

The results for the full set of geometries are shown in Fig. 14. Overall, all geometries follow the same general trend: as the number of microphones increases, the minimum and mean values rise, the maximum value stabilizes at 14 dB, and the min-to-max range narrows. However, this trend is not strictly monotonic, as increasing the number of microphones does not always yield better performance. For example, with the t-design geometry, at least 28 microphones are required for the minimum to exceed the 6 dB threshold. However, increasing the number of microphones to 32, 36, 42, or even 50 does not improve performance. The narrowest optimal min-to-max range with this geometry is achieved with 62 microphones, though comparable performance is obtained with 48 microphones, allowing a 25 % reduction in the number of microphones. Among the other geometries, the Spiral is the most efficient, maintaining MSR values above 6 dB from 28 to 64 microphones. The narrowest min-to-max range for this geometry occurs at 60 microphones. Conversely, the Maximal Volume and Minimum Energy geometries perform the worst.

The results for the limited set of geometries are displayed in Fig. 15. The minimum MSR value for the Equi-Angle, Gauss-Legendre, and Lebedev geometries requires at least 50 microphones to exceed the 6 dB threshold. In contrast, Fliege and B&K geometries achieve comparable performance with only 36 microphones. The Efficient t-design and L-design geometries are less effective than the Maximum Determinant and Fibonacci geometries. Notably, the Fibonacci geometry surpasses the 6 dB threshold with just 25 microphones. The narrowest min-to-max range is obtained with the Maximum Determinant geometry when using 64 microphones.

To conclude, increasing the number of microphones helps reduce sidelobe levels; however, this reduction is not monotonic and is highly dependent on geometry. Certain geometries, such as Maximal Volume and L-design, are not well suited for use with the CBF, whereas the Spiral geometry, with $Q \geq 28$, consistently provides array configurations with high minimum MSR values. This conclusion

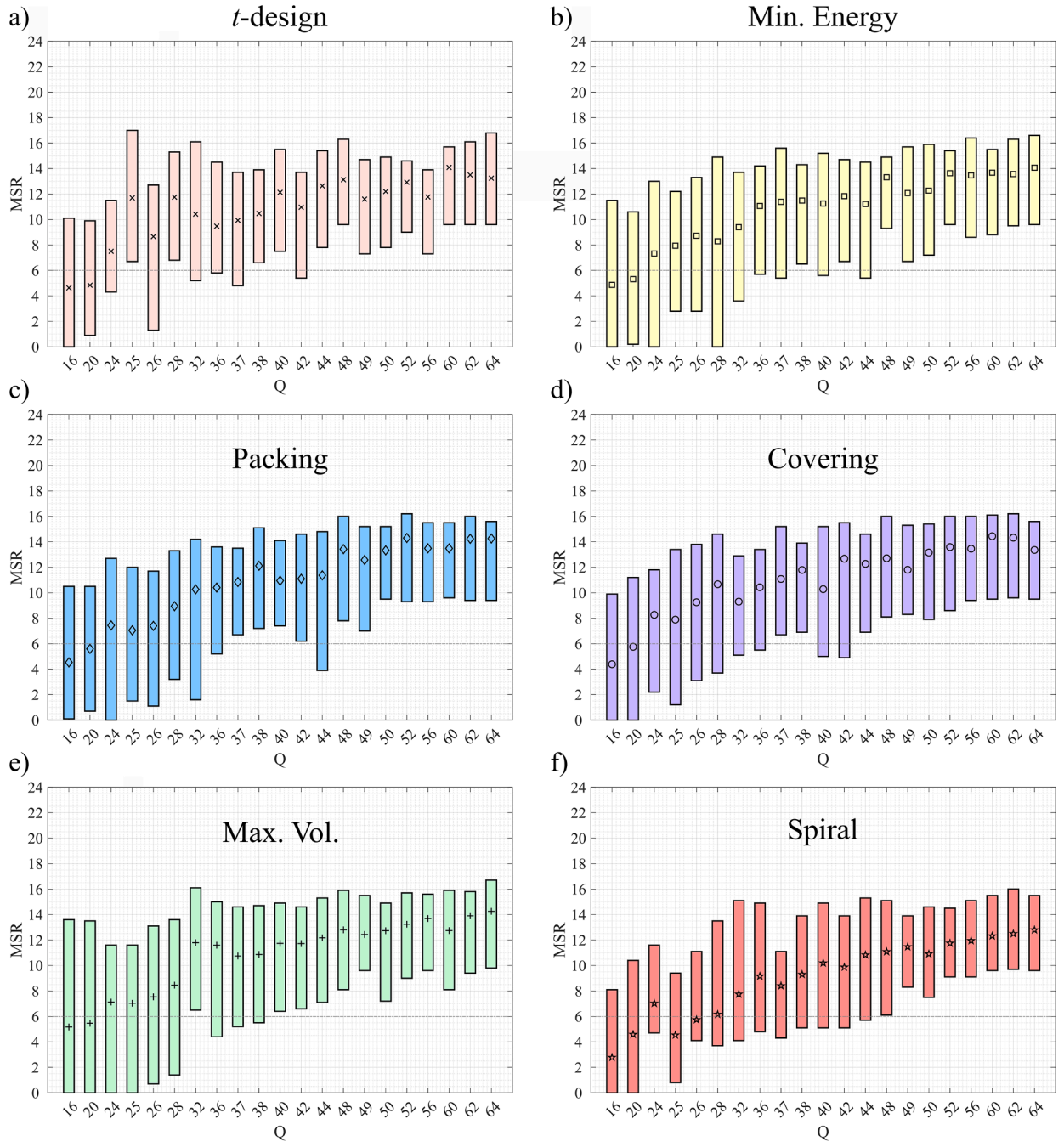

Fig. 16. MSR distribution obtained with the SHB algorithm and rigid SMAs (full set), as a function of the number of microphones Q: (a) × t-design, (b) □ Min. Ener., (c) ◇ Packing, (d) ○ Covering, (e) + Max. Vol. and (f) ☆ Spiral. The horizontal dotted line corresponds to MSR = 6 dB.

must, however, be interpreted within the context of the selected kr_a range. The presence of sidelobes reduces both the lower edge of the boxplot and the mean. With 64 microphones, MSR values are generally higher than with fewer microphones, leading to a natural upward shift and contraction of the box interval.

4.4.2. MSR Distribution with SHB

Fig. 16 presents the results for the full set of geometries. Again, the overall trend mirrors that observed with the CBF: the minimum, mean, and maximum values rise, and the min-to-max range becomes narrower as the number of microphones increases. Nevertheless, some geometries achieve a higher minimum value with fewer microphones. For instance, with the t-design geometry, the first mini-

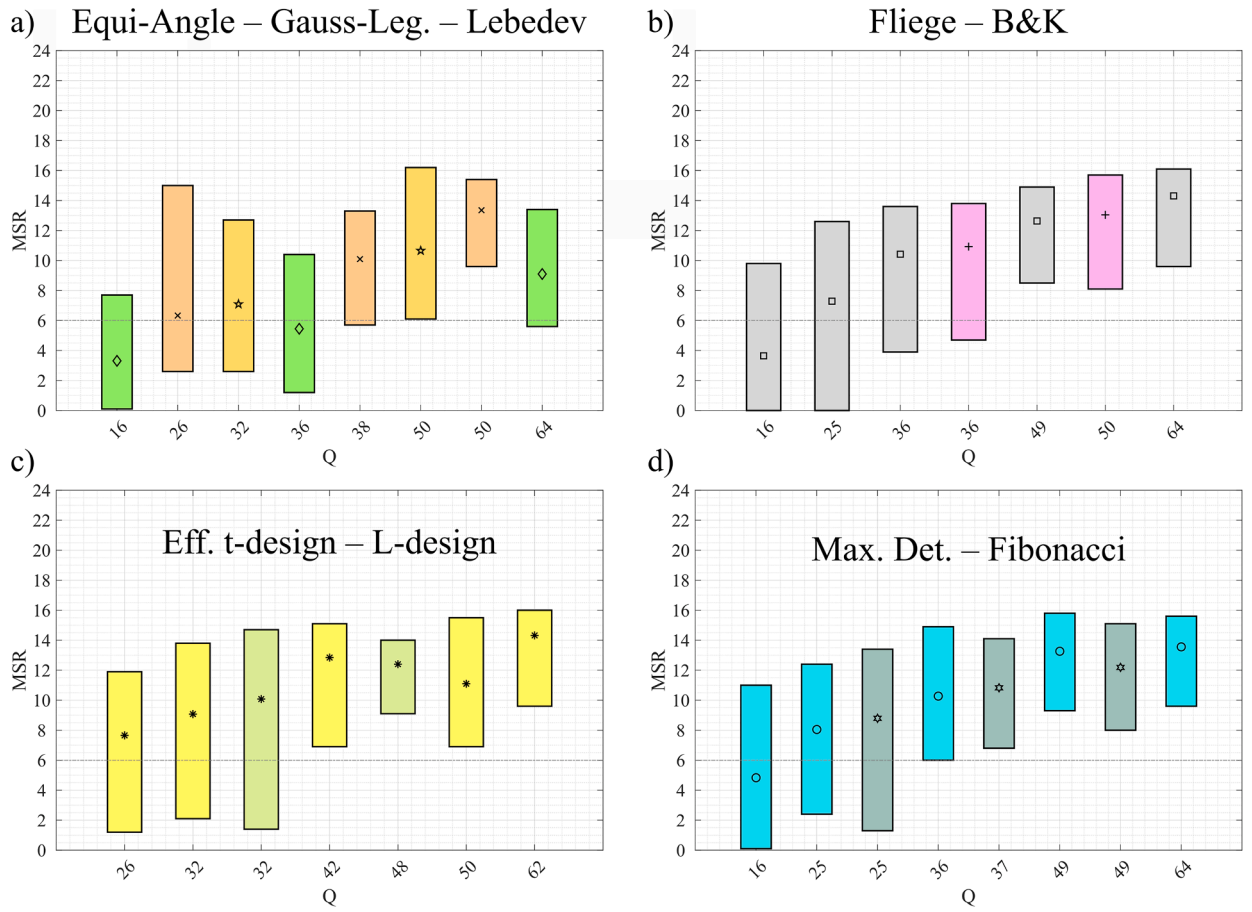

Fig. 17. MSR distribution obtained with the SHB algorithm and rigid SMAs (limited set), as a function of the number of microphones Q: (a) Eq. Angle, Gauss-Leg., Lebedev, (b) Fliege, B&K, (c) Eff. t-design, L-design and (d) Max. Det. and Fibonacci. The horizontal dotted line corresponds to MSR = 6 dB.

mum value exceeding the 6 dB threshold requires only 25 microphones. Additionally, the minimum value observed for 25 microphones surpasses those of 26, 32 to 38, and 42 microphones. The highest maximum value for the t-design geometry is also observed with 25 microphones. The highest minimum value is achieved with 64 microphones, while 60 microphones provide similar performance with a higher mean, and 48 microphones yield comparable results, offering a 25 % reduction in the number of microphones. The t-design geometry produces the greatest number of minimum values above the 6 dB threshold, followed by Packing and Maximal Volume. The Packing geometry exceeds the 6 dB threshold with just 32 microphones. Conversely, the Minimum Energy and Spiral geometries perform the worst, yielding the fewest MSR values above the 6 dB threshold.

Fig. 17 displays the results for the limited set of geometries. The Equi-Angle and Gauss-Legendre geometries yield the worst results, as none of the tested configurations exceeds the 6 dB threshold. The Lebedev geometry achieves the best performance within this set using 50 microphones. In contrast, the B&K geometry exhibits lower performance with 50 microphones compared to the Fliege geometry with 49 microphones. Nevertheless, the Fliege and B&K geometries are less effective than the Efficient t-design and L-design geometries, which require at least 42 and 48 microphones, respectively, to exceed the threshold. The Maximum Determinant geometry outperforms the Fibonacci geometry at 49 microphones.

To conclude, increasing the number of microphones contributes to lowering sidelobe levels; however, this decrease is neither monotonic nor uniform and strongly depends on the geometry. Some geometries, like Equi-Angle and Gauss-Legendre, are ineffective with SHB, whereas the t-design geometry yields the best results.

4.5. Discussion

The use of microphone arrays in professional environments involves specific constraints, particularly in terms of compactness and cost. These limitations restrict the feasible choices for the array radius and the number of microphones (see Table A.1 for a conversion of the kr_a values). Among the three evaluation criteria, the MSR is the most restrictive, as it validates a narrower operational range compared to the SAR and MLD criteria.

In this noise-free scenario, SHB is recommended in the low-frequency range ($kr_a \in [0, 1.5]$), as it provides a mainlobe width below 30 % of SAR and an MSR greater than 6 dB. However, in noisy conditions, this performance may be overly optimistic, since noise increases sidelobe levels, which can be mitigated by regularization. In the mid-frequency range ($kr_a \in [1.5, 6]$), either CBF or SHB can be used. In the high-frequency range ($kr_a \in [6, 16]$), both algorithms can be recommended, but a large number of microphones is required to achieve usable MSR as kr_a increases. When facing specific requirements in terms of source frequency range, array radius, geometry, or beamforming algorithm, the user may check the behavior of non-targeted parameters. For example, for an SMA with a radius of 0.10 m, the low-frequency range sets a frequency limit of around 800 Hz, where SHB with a rigid array is recommended. In the mid-frequency range, the applicable range is [800, 3150] Hz, and the Fliege geometry with 36 microphones can be recommended. Beyond this frequency, the Fliege geometry yields an MSR below 6 dB. Alternatively, the CBF algorithm with B&K geometry and an open array can be recommended from a mid- to high-frequency range with 36 microphones. Note that, for a fixed kr_a value, doubling the array radius corresponds to halving the frequency.

Finally, the comparative analysis over the kr_a range [2, 8] in Section 4.4 shows that the CBF algorithm, when combined with a Maximal Volume geometry comprising 64 microphones, yields the smallest variance. A viable alternative requiring fewer microphones is the 49-microphone Spiral or the 48-microphone *t*-design geometry. For configurations involving fewer than 36 microphones, the 28-microphone *t*-design geometry remains a robust option. With the SHB algorithm, the most consistent MSR performance across the investigated kr_a range is achieved using either the Efficient *t*-design or the Minimum Energy geometry with 48 microphones. When using fewer than 36 microphones, the *t*-design geometries with 25 or 28 microphones are recommended.

5. Conclusion

The study of spherical microphone arrays (SMAs) has gained significant attention in recent years, with numerous designs proposed in the literature. Many SMA designs have been studied in the literature, but a comprehensive performance analysis using CBF and SHB has been lacking. This study addresses this gap by systematically comparing various SMA geometries based on the dimensionless parameter kr_a and the number of microphones. The evaluation is conducted using objective criteria, including mainlobe level difference, mainlobe width (solid angle ratio), and mainlobe-to-sidelobe ratio, providing insights for practical applications and future research. The results of this study can be used to guide the selection of an optimal SMA for an application, considering constraints on array size and the number of microphones.

Acoustic images were obtained by numerical simulations of the sound field generated by a monopole source in free-field conditions. The SMAs of interest were either open or rigid. The aforementioned instrumental criteria were used to quantify the performance of the acoustic images obtained with either exactly 36 and 50 microphones, or with the closest available numbers, as a function of kr_a ranging from 0.1 to 16. Furthermore, acoustic images were analyzed using the mainlobe-to-sidelobe ratio distribution of the data as a function of the number of microphones ranging from 16 to 64.

Based on the mainlobe level difference, open SMAs are recommended for CBF, as they avoid errors in source-strength estimation caused by scattering at the microphone body of rigid SMAs. By contrast, with the SHB algorithm, rigid SMAs are generally recommended because open SMAs, without additional processing or modifications to the array layout, induce significant localization errors due to numerical instabilities. Additionally, the Equi-Angle and Gauss-Legendre geometries are not recommended for use with SHB, as their performance is less effective than that of the other geometries with comparable numbers of microphones.

Based on the mainlobe level difference and the solid angle ratio, the results of the CBF algorithm with an open SMA remain consistent across various geometries, unlike those of the SHB with a rigid SMA. According to the solid angle ratio, CBF is not recommended for $kr_a < 1.3$, where the mainlobe occupies more than 30 % of the acoustic image. Instead, SHB should be used at these kr_a values to achieve a narrower mainlobe when filter regularization can be omitted due to the absence of measurement noise. Increasing the number of microphones from $36^\star$ to $50^\star$ improves performance at higher kr_a values.

According to the analysis of the mainlobe-to-sidelobe ratio distribution, with CBF and open SMAs, the Spiral or *t*-design geometry is recommended, as they achieve the highest minimum mainlobe-to-sidelobe ratios. With SHB, a geometry with equidistantly placed microphones is recommended, which is obtained with the *t*-design. The optimal choice always depends on a trade-off between radius constraints, target frequency, and the number of microphones.

The provided source code would allow further assessments of the beamforming methods in more practical acoustic scenarios involving multiple sound sources and sensor or environmental noise.

Declaration of generative AI and AI-assited technologies in the writing process

During the preparation of this work, the authors used ChatGPT in order to improve language and readability. After using this tool, the authors reviewed and edited the content as needed and take full responsibility for the content of the publication.

CRediT authorship contribution statement

Kévin Rouard: Writing – review & editing, Writing - original draft, Visualization, Validation, Software, Methodology, Investigation, Formal analysis, Data curation, Conceptualization; **Julien St-Jacques:** Writing – review & editing; **Loïc Forma:** Writing – review & editing; **Loic Boileau:** Writing – review & editing; **Franck Sgard:** Writing – review & editing, Validation, Supervision, Resources, Project administration, Funding acquisition; **Olivier Doutres:** Writing – review & editing, Validation, Supervision, Resources, Project administration, Funding acquisition; **Nicolas Quaegebeur:** Writing - review & editing; **Hugues Nélisse:** Writing - review & editing;

François Grondin: Writing – review & editing; **Thomas Padois:** Writing – review & editing, Validation, Supervision, Resources, Project administration, Funding acquisition, Conceptualization.

Data availability

Data and codes are mentioned in the manuscript.

Declaration of competing interest

The authors declare that they have no known competing financial interests or personal relationships that could have appeared to influence the work reported in this paper.

Funding

This research was supported by the Institut de recherche Robert-Sauvé en santé et en sécurité du Travail (grant number 2018-0026) and Mitacs (IT25827).

Appendix A.

Table A.1 provides the conversion of the dimensionless number kr_a into frequency and radius. To read this table, the reader may choose a frequency and radius to find the corresponding kr_a value at the intersection of the two values. The results of acoustic imaging with the same ratio kr_a are identical. For example, an acoustic image with an SMA geometry of radius $r_a = 0.40$ m at 200 Hz is identical to one with the same geometry at radius $r_a = 0.10$ m at 800 Hz.

Table A.1
The dimensionless number kr_a is defined as the product of the radius r_a and the wavenumber $k = 2\pi f/c$, where f is the frequency and $c = 343\ \mathrm{ms}^{-1}$ is the speed of sound.

kr_a	*Radius (m)*			
Frequency (Hz)	0.04	0.10	0.20	0.40
200	0.15	0.37	0.73	1.47
250	0.18	0.46	0.92	1.83
315	0.23	0.58	1.15	2.31
400	0.29	0.73	1.47	2.93
500	0.37	0.92	1.83	3.66
630	0.46	1.15	2.31	4.62
800	0.59	1.47	2.93	5.86
1000	0.73	1.83	3.66	7.33
1250	0.92	2.29	4.58	9.16
1600	1.17	2.93	5.86	11.72
2000	1.47	3.66	7.33	14.65
2500	1.83	4.58	9.16	18.32
3150	2.31	5.77	11.54	23.08
4000	2.93	7.33	14.65	29.31
5000	3.66	9.16	18.32	36.64
6300	4.62	11.54	23.08	46.16
8000	5.86	14.65	29.31	58.62

References

[1] C. Noël, V. Planeau, D. Habault, A new temporal method for the identification of source directions in a reverberant hall, J. Sound Vib. 296 (3) (2006) 518–538. https://doi.org/10.1016/j.jsv.2005.12.056
[2] G. Battista, P. Chiariotti, P. Castellini, Spherical harmonics decomposition in inverse acoustic methods involving spherical arrays, J. Sound Vib. 433 (2018) 425–460. https://doi.org/10.1016/j.jsv.2018.05.001
[3] L. Lamotte, T. Le Magueresse, H. Siwiak, Experimental validation of source quantification methods using a rigid spherical microphone array, e-Forum Acusticum, 2020, pp. 801–804. https://doi.org/10.48465/FA.2020.0271
[4] P. Chiariotti, M. Martarelli, P. Castellini, Acoustic beamforming for noise source localization - reviews, methodology and applications, Mech. Syst. Signal Process. 120 (2019) 422–448. https://doi.org/10.1016/j.ymssp.2018.09.019
[5] G. Heilmann, A. Meyer, D. Döbler, Time-Domain beamforming using 3D-microphone arrays, in: Bebec, 2008.
[6] A. Djordjevic, M. Licanin, Construction, calibration, evaluation of spherical microphone array and its application for beamforming, in: Inter-Noise Noise-Con Congr. Conf. Proc., 2016, pp. 4598–4609.
[7] T. Padois, F. Sgard, O. Doutres, A. Berry, Acoustic source localization using a polyhedral microphone array and an improved generalized cross-correlation technique, J. Sound Vib. 386 (2017) 82–99. https://doi.org/10.1016/j.jsv.2016.09.006
[8] T. Padois, O. Doutres, F. Sgard, A. Berry, Optimization of a spherical microphone array geometry for localizing acoustic sources using the generalized cross-correlation technique, Mech. Syst. Signal Process. 132 (2019) 546–559. https://doi.org/10.1016/j.ymssp.2019.07.010

[9] K. Haddad, J. Hald, 3D Localization of acoustic sources with a spherical array, in: EuroNoise - SFA, 123, 2008, pp. 1585–1590. https://doi.org/10.1121/1.2933754
[10] J. Hald, Spherical beamforming with enhanced dynamic range, SAE Int. J. Passeng. Cars - Mech. Syst. 6 (2) (2013) 1334–1341. https://doi.org/10.4271/2013-01-1977
[11] F.H. Araujo, F.A. Pinto, Comparison between the spherical harmonics beamforming and the delay-and-Sum beamforming, in: Inter-Noise Noise-Con Congr. Conf. Proc., 253, 2016, pp. 1007–1017.
[12] J. Merimaa, Applications of a 3-d microphone array, in: Audio Eng. Soc. Conv. Paper, 5501, 2002.
[13] A. Parthy, C. Jin, A. van Schaik, Measured and theoretical performance comparison of a co-centred rigid and open spherical microphone array, in: ICALIP, IEEE, 2008, pp. 1289–1294. https://doi.org/10.1109/ICALIP.2008.4590251
[14] C. Cariou, O. Delverdier, S. Paillasseur, L. Lamotte, Tool for interior noise sources detection in aircraft with comparison of configurations, in: Bebec, 2012.
[15] C.T. Jin, N. Epain, A. Parthy, Design, optimization and evaluation of a dual-Radius spherical microphone array, IEEE/ACM Trans. Audio Speech Lang. Process. 22 (1) (2014) 193–204. https://doi.org/10.1109/TASLP.2013.2286920
[16] T. Padois, J. St-Jacques, K. Rouard, N. Quaegebeur, F. Grondin, A. Berry, H. Nélisse, F. Sgard, O. Doutres, Acoustic imaging with spherical microphone array and kriging, JASA Express Lett. 3 (4) (2023) 042801. https://doi.org/10.1121/10.0017790
[17] T. Padois, J. Fischer, C. Doolan, O. Doutres, Acoustic imaging with conventional frequency domain beamforming and generalized cross-correlation: a comparison study, App. Acoust. 177 (2021) 107914. https://doi.org/10.1016/j.apacoust.2021.107914
[18] K. Rouard, J. St-Jacques, F. Sgard, H. Nelisse, A. Berry, N. Quaegebeur, F. Grondin, O. Doutres, T. Padois, Numerical comparison of acoustic imaging algorithms for a spherical microphone array, in: Bebec, 2022.
[19] T. Padois, O. Doutres, F. Sgard, A. Berry, Time domain localization technique with sparsity constraint for imaging acoustic sources, Mech. Syst. Signal Process. 94 (2017) 85–93. https://doi.org/10.1016/j.ymssp.2017.02.035
[20] B. Rafaely, Fundamentals of Spherical Array Processing, number 16 in Springer Topics in Signal Processing, Springer International Publishing : Imprint: Springer, 2nd ed. 2019 edition, 2019. https://doi.org/10.1007/978-3-319-99561-8
[21] B. Rafaely, Fundamentals of Spherical Array Processing, (2024). https://www.mathworks.com/matlabcentral/fileexchange/68655-fundamentals-of-spherical-array-processing.
[22] I. Balmages, B. Rafaely, Open-sphere designs for spherical microphone arrays, IEEE Trans. Audio Speech Lang. Process. 15 (2) (2007) 727–732. https://doi.org/10.1109/TASL.2006.881671
[23] B. Rafaely, Phase-mode versus delay-and-Sum spherical microphone array processing, IEEE Signal Process. Lett. 12 (10) (2005) 713–716. https://doi.org/10.1109/LSP.2005.855542
[24] T. Padois, O. Doutres, F. Sgard, A. Berry, On the use of geometric and harmonic means with the generalized cross-correlation in the time domain to improve noise source maps, J. Acoust. Soc. Am. 140 (1) (2016) EL56–EL61. https://doi.org/10.1121/1.4955007
[25] Z. Chu, Y. Yang, Y. He, Deconvolution for three-Dimensional acoustic source identification based on spherical harmonics beamforming, J. Sound Vib. 344 (2015) 484–502. https://doi.org/10.1016/j.jsv.2015.01.047
[26] C. Du, Q. Leclere, B. Li, Design and evaluation of open spherical microphone arrays, in: ICSV, 2017.
[27] B. Rafaely, Analysis and design of spherical microphone arrays, IEEE Trans. Speech Audio Process. 13 (1) (2005) 135–143. https://doi.org/10.1109/TSA.2004.839244
[28] E. Sarradj, Three-dimensional acoustic source mapping with different beamforming steering vector formulations, Adv. Acoust. Vib. 2012 (2012) 1–12. https://doi.org/10.1155/2012/292695
[29] E.G. Williams, 8.8.4 Neuman green function for the exterieur problem on a sphere, in: Fourier Acoustics: Sound Radiation and Nearfield Acoustical Holography, Academic Press, 1999.
[30] W. Song, W. Ellermeier, J. Hald, Using beamforming and binaural synthesis for the psychoacoustical evaluation of target sources in noise, J. Acoust. Soc. Am. 123 (2) (2008) 910–924. https://doi.org/10.1121/1.2822669
[31] J. St-Jacques, K. Rouard, F. Sgard, H. Nélisse, A. Berry, N. Quaegebeur, F. Grondin, L. Boileau, O. Doutres, T. Padois, Effect of the error on the sound speed and microphone position on acoustic image obtained with a spherical microphone array, in: Proc. AWC, 50–3, 2022, p. 132.
[32] R.H. Hardin, N.J.A. Sloane, Mclaren's improved snub cube and other new spherical designs in three dimensions, Discrete Comput. Geom. 15 (4) (1996) 429–441. https://doi.org/10.1007/BF02711518
[33] N.J.A. Sloane, Home Page, (2025). http://neilsloane.com/.
[34] P. Lecomte, P.-A. Gauthier, C. Langrenne, A. Berry, A. Garcia, A fifty-Node lebedev grid and its applications to ambisonics, J. Audio Eng. Soc. 64 (11) (2016) 868–881. https://doi.org/10.17743/jaes.2016.0036
[35] J.H. Conway, N.J.A. Sloane, Sphere Packings, Lattices and Groups, 290 of *Grundlehren Der Mathematischen Wissenschaften*, Springer-Verlag New York, third edition, 1999.
[36] R.H. Hardin, N.J.A. Sloane, Codes (spherical) and designs (experimental), Proc. Symposia Appl. Math. 50 (1995) 177–206.
[37] R. Swinbank, R. James Purser, Fibonacci grids: a novel approach to global modelling, Quarterly J. Royal Meteorol. Soc. 132 (619) (2006) 1769–1793. https://doi.org/10.1256/qj.05.227
[38] J. Burkardt, Fibonacci Spiral Grid on a Sphere, 2019, https://people.math.sc.edu/Burkardt/m_src/sphere_fibonacci_grid/sphere_fibonacci_grid.HTML.
[39] I.V. Lebedev, N.D. Laikov, A quadrature formula for the sphere of the 131st algebraic order of accuracy, Doklady Math. 59 (3) (1999) 477–481.
[40] J. Burkardt, Quadrature Rules for the Sphere, 2010, https://people.sc.fsu.edu/~jburkardt/datasets/sphere_lebedev_rule/sphere_lebedev_rule.HTML.
[41] J. Fliege, U. Maier, The distribution of points on the sphere and corresponding cubature formulae, IMA J. Numer. Anal. 19 (2) (1999) 317–334. https://doi.org/10.1093/imanum/19.2.317
[42] R. Womersley, Interpolation and Cubature on the Sphere, 2020, https://web.maths.unsw.edu.au/~rsw/Sphere.
[43] Z. Chu, S. Zhao, Y. Yang, Y. Yang, Deconvolution using CLEAN-SC for acoustic source identification with spherical microphone arrays, J. Sound Vib. 440 (2019) 161–173. https://doi.org/10.1016/j.jsv.2018.10.030
[44] G. Moreno, Spherical Nearfield Acoustical Holography, Master's thesis, Technical University of Denmark, 2008.
[45] R.S. Womersley, Efficient Spherical Designs with Good Geometric Properties, 2017. arXiv preprint. arXiv:1709.01624
[46] C. Puhle, Spherical acoustical holography using planar microphone arrays, in: Bebec, 2020, p. 15.
[47] R.S. Womersley, I.H. Sloan, How good can polynomial interpolation on the sphere be ?, Adv. Comput. Math. 14 (2001) 195–226.
[48] G. Wright, A Collection of Matlab Functions for Experimenting with Different Point Sets on the Sphere, 2018. https://github.com/gradywright/spherepts.
[49] A. Pereira, Acoustic Imaging in Enclosed Spaces, Ph.D. thesis, INSA de Lyon, 2013.
[50] S.O. Petersen, Localization of Sound Sources Using 3D Microphone Array, 2004, http://www.oscarpetersen.dk/speciale/Thesis.pdf.
[51] E. Arcondoulis, Y. Liu, An iterative microphone removal method for acoustic beamforming array design, J. Sound Vib. 442 (2019) 552–571. https://doi.org/10.1016/j.jsv.2018.11.005
[52] K. Rouard, J. St-Jacques, F. Sgard, O. Doutres, H. Nélisse, L. Boileau, A. Berry, N. Quaegebeur, F. Grondin, T. Padois, A criterion based on the calculation of a solid angle to assess the quality of acoustic images obtained with a SMA, in: J. Can. Acoust. Assoc., 2023.
[53] K. Tikuišis, Peaks2 - Find Peaks in 2D Data without Additional Toolbox, 2023, https://www.mathworks.com/matlabcentral/fileexchange/113225-peaks2-find-peaks-in-2d-data-without-additional-toolbox.